JOURNAL OF APPLIED ELECTROCHEMISTRY 24 (1994) 835–857

Integrity of ultramicro-stimulation electrodes determined from electrochemical measurements

U. M. TWARDOCH

EIC Laboratories Inc., 111 Downey Street, Norwood, MA 02062, USA

Received 19 April 1993; revised 15 January 1994

Methods to control the quality of stimulation electrodes for human patients are desirable. The results of a comparative electrochemical evaluation of three types of ultramicroelectrodes presently used for neural stimulation are discussed. The iridium electrodes examined were fabricated from iridium wire or by thin film technology. Electrochemical protocols based on single cyclic voltammetry are proposed for quality control. Defective insulator–conductor seals have been modelled and the simulation provides the basis for the protocol. The porous metal produced by thin film methodology is detected. The consequences of these defective structures for activation to hydrous iridium oxide coated electrodes for neural stimulation are discussed.

List of symbols

A	surface area of an electrode (cm^2)
A_{cav}	surface area of electrode within a cavity (cm^2)
A_{exp}	exposed surface area of electrode, i.e. accessible for electroactive species by diffusion (cm^2)
A_p	peripheral surface area of electrode, i.e. accessible only for charging process (cm^2)
A_T	total measured surface area of electrode (cm^2)
a	dimensionless quantity, $nF\nu/RT$
b	length of cylindrical electrode (cm)
C	concentration ($mol\,cm^{-3}$)
C_{dl}	double layer capacitance, $F\,cm^{-2}$
C_d	capacitance $C_{dl} \times A$, of an electrode (F)
C_0^b	bulk concentration of oxidized species ($mol\,cm^{-3}$)
D	diffusion coefficient ($cm^2\,s^{-1}$)
d	superficial diameter of electrode (cm)
E	potential of an electrode versus a reference electrode (V)
$E_{m/2}$	half maximum potential, i.e. potential where $i = i_{m/2}$ (V)
$E^{0\prime}$	formal potential of an electrode against a reference electrode (V)
E_p	peak potential, i.e. potential where $i = i_p$ in cyclic voltammetry (V)
$E_{p/2}$	half peak potential, i.e. potential where $i = i_{p/2}$ (V)
ESA	electrochemically determined surface area of an electrode (cm^2)
F	Faraday's constant, $96\,485\,C\,mol^{-1}$
f_{th}	film thickness (cm)
GSA	geometrically determined surface area of an electrode (cm^2)
h	altitude of the cone electrode (cm)
i	current (A)
i_p	peak current (A)
i_{ss}	steady state current (A)
k	heterogeneous rate constant ($cm\,s^{-1}$)
n	number of electrons in electrode process
n_α	number of electrons in rate determining step
p	dimensionless parameter, i.e. $r_d(nF\nu/RTD)^{1/2}$
R	gas constant, $8.314\,J\,mol^{-1}\,K^{-1}$
R_u	uncompensated resistance (Ω)
r_c	(i) basal radius of a cone electrode (cm), (ii) radius of the cylindrical electrode (cm)
r_d	radius of the disc electrode (cm)
T	Temperature (K)
t	time (s)
V	volume of the electrolyte in cavity (cm^3)
y	depth of a cavity (cm)

Greek symbols

α	transfer coefficient
δ	diffusion layer thickness (cm)
λ	width of a cavity (cm)
ν	scan rate ($V\,s^{-1}$)
ϕ	normalized current for the spherical electrode with the contribution due to finite volume in cyclic voltammetry
ϕ_{max}	maximum value of the normalized current for the spherical electrode with the contribution due to finite volume in cyclic voltammetry
χ	current function for linear diffuse i.e. normalized current in cyclic voltammetry
ψ	normalized current in the absence of mass transfer in cyclic voltammetry
ζ	contribution due to spherical diffusion to the normalized current in cyclic voltammetry

1. Introduction

Microelectrodes are used in physiology and their use for neural stimulation is widely accepted in medicine [1]. Microelectrodes in these contexts have been either individual or multiple combinations of electrodes whose dimensions are of the order of micrometres. In the electrochemical literature, microelectrodes are often renamed ultramicroelectrodes. Present and future implementation of such electrodes or novel

0021-891X

electrode arrays for neural prostheses and other applications requires, *inter alia*, a comparative study of electrode designs. A knowledge of the electrode's geometry and the real surface area of the stimulation electrode is vital to select the safe charge injection limit. Recent work by Fleischmann [2], Heinze [3], Oldham [4, 5], and others [6, 7] has led to the development of working equations describing the electrochemical behaviour for several ultramicroelectrode geometries from which the pertinent electrode dimensions can be extracted. Physiological and medical applications can be major benefactors from these electrochemical developments.

A case in point is the use of ultramicroelectrodes for neural stimulation, where pulsed currents are used to stimulate and study neural activity [8]. Although a recent major goal in neurostimulation has been to develop smaller electrodes that can inject a charge necessary to stimulate neuronal activity without electrochemical contamination of local tissue, the issues associated with the definition of real surface area have been largely ignored. The main improvement in selectivity by neural stimulation, for example, arises when the size of the ultramicroelectrode or an array is comparable to, or smaller than a single neuron. The question then arises, for a typical pulse length [9], as to the proper magnitude of the current density required to stimulate the neuron(s). At least two factors need to be considered: (a) the intrinsic properties of the neural system and (b) the electrode designs to be employed in such work [9]. In answering this question, the means by which the charge is injected as well as characteristics of the stimulation electrode are critical.

The electrical excitation of the neurons requires a change of the transmembrane potential, activated by a resultant electrical field induced, preferably, without electrolytic alteration of the composition of the local neuronal medium [8]. Charge injection has been achieved by the following, substantially different, approaches.

(i) *Charge injection under conditions where no electron transfer occurs across the electrode–solution interface.* In aqueous media, the ideally polarizable potential range of a solid electrode is limited and the corresponding charge density is too low to excite a neuron. An increase in the capacitance and effectively the charge density per geometric surface area, achieved by roughening the electrode surface, is limited by a concomitant decrease in pore size, and a corresponding increase in the iR drop within the pores that mitigates against further contributions by increased internal surface area.

(ii) *Charge injection utilizing the pseudocapacitance associated with a monomolecular-layer of electroactive species.* The charge densities from 200 to 400 $\mu C\,cm^{-2}$ [10–12] are an order of magnitude greater than those for approach (i). However, in contrast to the double-layer charging process, the electrochemical adsorption process will be limited by the finite value of the rate constants for either the electron transfer or the adsorption/desorption processes.

(iii) *Charge injection via redox processes associated with transition metal, micro porous, hydrous oxide films.* Noble metals such as iridium and ruthenium form hydrous oxides films that are often formulated as IrO_x and RuO_x. The redox reactions of these oxides involve, *inter alia*, the migration of ions, and the overall process is limited by the mass transport of these species within the film [13, 14].

For all these approaches, at high frequencies, the limit, is the double-layer charge, proportional to the 'real' surface area. Thus, it is imperative that the electrode surface is properly characterized prior to implantation. The individual electrode, or elements in an array should have a well defined surface that has a definitive chemical composition that is stable under the prevailing, *in vivo*, conditions. These requirements must be met for simple recording electrodes to ensure the accessibility of the electrode to the electrical field generated by the neuron(s). For a stimulation electrode, it is important to evaluate the electric field evoked in the electrode-neuronal *interphase* by the 'real' applied current density. The reproducibility of the charge injection process can be compromised by changes in surface composition due to intergranular migration of elements from any bonding underlayer used, [15–17]. A major source of electrode instability that can lead to distortion of these electric fields arises from imperfections that develop in the seal between the conducting electrode and the insulator. The penetration of electrolyte solution, for example, cerebral spinal fluid, between the conductor and the insulator may have unpredictable consequences!

Prevailing designs for electrode surfaces use different geometries that take into account the need to penetrate tissue. To a first approximation, these geometries can be likened to those of a cone or a disc. In stimulation it is imperative to know or determine the actual geometry of the electrode because the *distribution* of the current across the electrode depends on the shape of the active surface. This is a critical design factor since the current density required for stimulation depends on the location of the electrodes. Although manufacturers of available electrodes carry out simple quality control measures, these are often insufficient to identify potential repercussions associated with the materials, the geometry of the electrodes and the nature of the pulsing regimes. The deficiencies in such quality control can result in undesirable responses when the electrodes are employed in biological and electrochemical experimentation.

The development of ultramicroelectrodes for neural recording and stimulation is often held back by the lack of suitable construction materials and the difficulties associated with their fabrication and manufacture. Some of these challenges have been solved during the past 20 years [18, 19]. Problems associated with the definition and stability of the

electrochemical surface of the electrode element continues to frustrate their development and deployment. The correlation of results obtained with the numerous electrode designs incorporating different geometries, construction materials and active electrode surfaces is handicapped by the lack of standardized protocols.

The characterization of the electrode surface and its geometric dimensions is an important objective in a more general scheme to optimize electrode designs. This paper reports an electrochemical investigation of iridium based ultramicroelectrodes of the types used in neural stimulation. The work included an evaluation of the quality of the seal at the conductor/insulator junction, the extent of electrolyte penetration into this junction and the effective electrochemically accessible surface area. The identification of major defects in the seals anticipates gross electrode failure. The results demonstrate some electrochemically important problems that can arise with these electrode designs, illustrate the advantages of the application of current ultramicroelectrode theories' to interpret the data in a way that reveals the benefits and limitations of the electrode designs, and targets where improvements in design and fabrication should be made.

2. Experimental details

The following three types of electrodes were characterized. (i) Huntington Medical Research Institute, provided two different electrodes fabricated from annealed iridium wire [20, 21]. The working surface was a bevelled cross section. The electrodes had geometric surface areas of 477 μm^2 and 7 μm^2 and were coded HMRI-IC-06-02 and HMRI-IC-05-06, respectively. (ii) University of Michigan, provided two lithographically prepared probes, each with five electrode sites [17]. The nominal geometric surface areas for the sites were 1000 μm^2 and 100 μm^2.

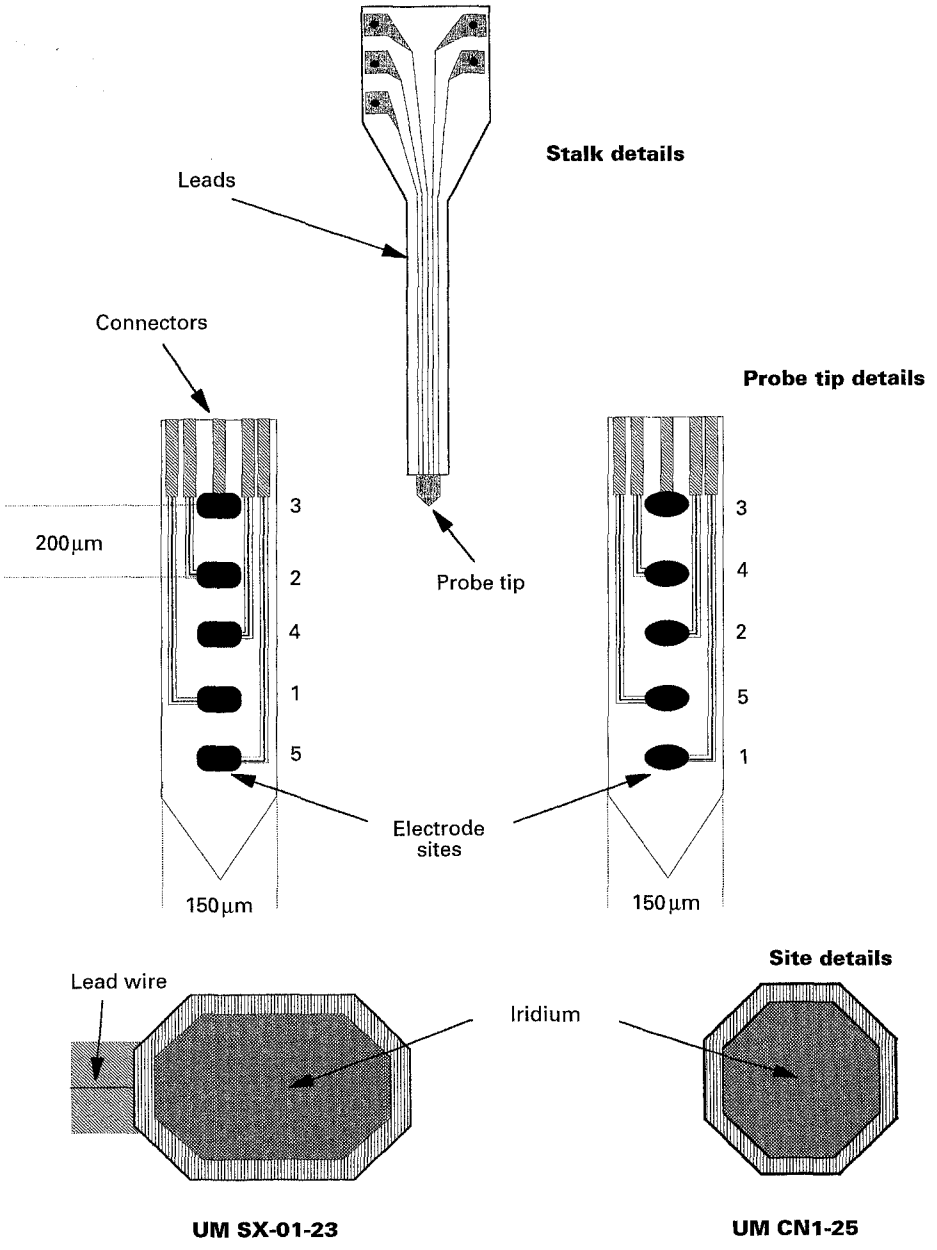

Fig. 1. Schematic of the iridium ultramicroelectrodes UM SX01 probe 23 and UM CN1 probe 25.

The electrode material was sputtered iridium. The probes were coded UM-SX-01 Probe 23 (1000 μm^2) and UM-CN1 Probe 25 (100 μm^2) and the individual electrode sites were numbered 1 to 5. The geometric layout and probe dimensions are shown in Fig. 1. (iii) Micro Probe, (Clarksburg, MD 20871) supplied six electrodes that had part numbers IR300310A and IR300320A. The working electrodes were etched iridium cones defined with a Parylene C insulator [9, 22, 23]. The individual electrodes were coded for the 10 μm electrodes as 10–1, 10–2, 10–3 and the 20 μm electrodes as 20–1, 20–2, 20–3.

Electrodes were evaluated in phosphate-buffered saline (PBS) alone and in PBS containing between 0.4 mM and 3.3 mM ruthenium hexaammine tris chloride, with the pH approximately 7.2. The electrochemical cell was a 25 mL vial and a Kel-F cell top, (BAS, Bioanalytical Systems Inc). The counter electrode was a 1.5 cm^2 platinum spiral. A BAS reference electrode: Ag|AgCl|NaCl 3 M|| was isolated from the main compartment by a Luggin capillary. Additional working electrodes included commercial, BAS, inlaid gold disk electrodes, 1.6 mm and 10 μm in diameter.

The electrochemical instrumentation was based on an Amel 551 potentiostat, modulated by a PAR 175 Universal Programmer. For currents below the minimum sensitivity level of the potentiostat, a BAS Model MF 2200 current amplifier was employed. Transients were recorded with a B-T 5120 microprocessor controlled recorder. The electrochemical cell was located inside a Faraday cage and the electrolyte was deoxygenated by a flow of argon.

For voltammetric measurements, the potential of the working electrode was varied between 0.2 and −0.4 V from an initial potential of 0.1 V against the reference electrode. The ruthenium complex undergoes a reversible, one electron reduction. The scan rates were selected on the basis of the geometry of the particular electrode so that changes in the mass transport from nonlinear to semiinfinite linear diffusion could be observed. The voltammograms acquired in the solutions of $Ru(NH_3)_6Cl_3$ in PBS were corrected for the charging and residual currents. As necessary, the electrodes were appraised by optical (Unitron Series N) and scanning electron microscopy, (Cambridge Instrument Stereoscan 120).

3. Results and discussion

Electrodes, representative of three approaches to electrode design, were the subject of this investigation. All the electrodes were fabricated from iridium metal. In stimulation applications, the working surfaces would have been converted into an iridium oxide film, but the iridium oxide film was *not* developed since it was the properties of the underlying electrode structure that were of particular interest.

The stability of all electrodes toward exposure to typical bioelectrolyte solutions (PBS) was assessed and their electrochemical surface areas determined. While a number of methods for surface area determination have been proposed [24], two methods were chosen based upon the application of a triangular potential waveform to an electrode exposed either to a supporting electrolyte or to supporting electrolyte containing depolarizer. The electrochemical reaction of the selected depolarizer, ruthenium hexaammine tris chloride, involves the reversible formation of a soluble product whose diffusion coefficient differs but little from that of the depolarizer. Using microelectrode discs and bands of known area, independent measurements on this depolarizer in the PBS supporting electrolyte at 23 ± 2 °C provided the characteristic data assembled in Table 1.

3.1. *General assessment*

Single cyclic voltammetry provided the initial assessment of the stability of each electrode in the aqueous electrolyte. It was found, experimentally, that the quality of an electrode is established by monitoring the reproducibility of the voltammetric responses, acquired at 0.050 $V s^{-1}$, for a solution of the ruthenium hexaammine cation in phosphate buffered saline over a two hour period. Figure 2 illustrates the situations observed for the UM probes CN1 and SX01. While the SX01 probe showed reproducible behaviour over this observation period and beyond, the voltammograms obtained for probe CN1 site 1 were distorted after only 10 min in contact with the electrolyte and the distortion became more severe as the contact time increased. All sites of the UM-CN1 behaved similarly. The Microprobe electrodes 10–2 and 20–2 showed continuous temporal changes. During the two hour

Table 1. Electrochemical properties of the ruthenium hexaammine ion in phosphate-buffered saline solution

Electrode property	*Platinum 24 °C error (8 pts)*	*Gold 22–24 °C error (8 pts)*	*Iridium 24 °C error (7 pts)*
$-i_p/AC\nu^{1/2}$/A cm mol^{-1} $V^{-1/2}$ $s^{1/2}$	687 ± 5	692 ± 17	688 ± 6
^cE_p/V	−0.228 ± 0.005	−0.225 ± 0.008	−0.232 ± 0.004
$^cE_{p/2}$/V	−0.169 ± 0.002	−0.166 ± 0.006	−0.170 ± 0.000
$^aE_p - {}^cE_p$/V	0.066 ± 0.008	0.071 ± 0.005	0.071 ± 0.007
$^cE_{p/2} - {}^cE_p$/V	0.059 ± 0.007	0.059 ± 0.002	0.062 ± 0.004

For the gold electrode, four different concentrations of depolarizer were used.
Potential against Ag|AgCl|3 M NaCl|| reference electrode.

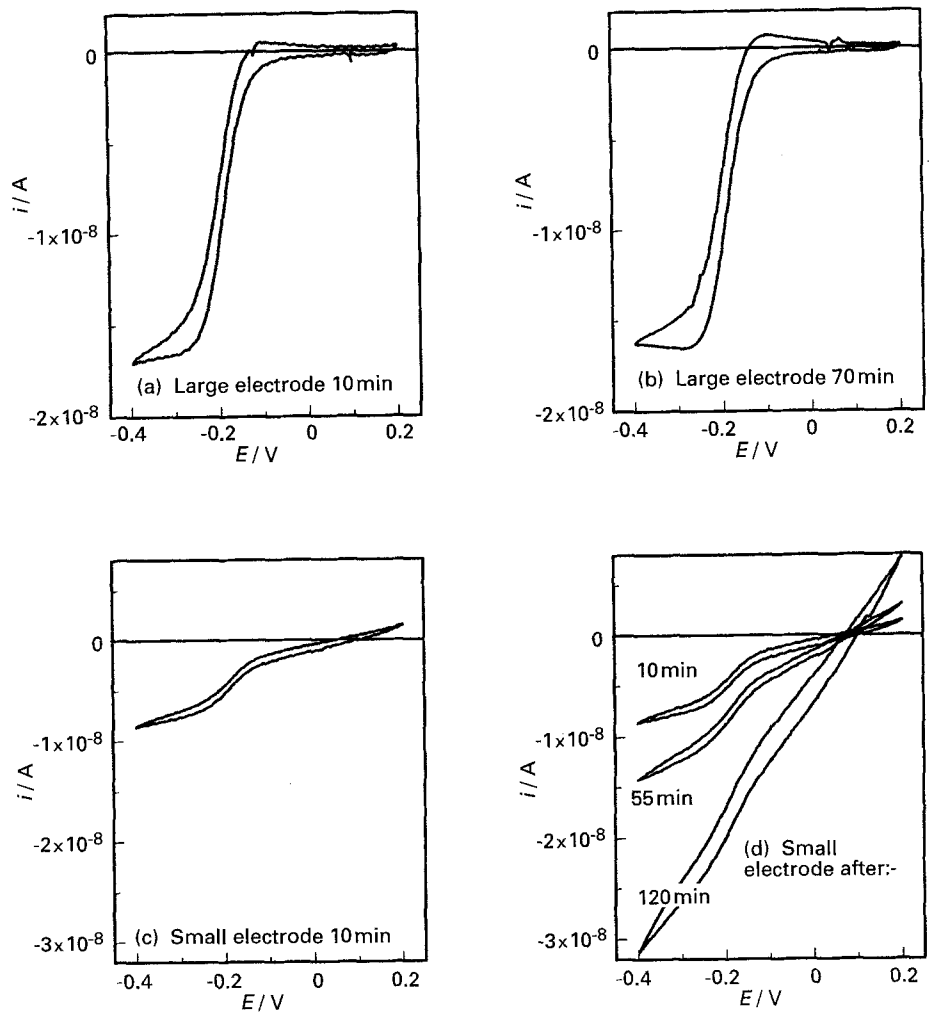

Fig. 2. The reproducibility of voltammetric responses acquired at 50 mV s^{-1} on UM SX-01 probe 23 site 1, $GSA = 10^{-5}$ cm^2, (a) and (b) and on UM CN1 probe 25 site 1, $GSA = 10^{-6}$ cm^2, (c) and (d), in 3.3 mM $Ru(NH_3)_6Cl_3$ in PBS. The times shown are the elapsed time after entry into the electrolyte.

test period, the voltammograms acquired with Microprobe electrodes, 10–1 and 20–3, were reproducible, however, the voltammetric currents increased by a fixed increment during the subsequent data acquisition. After this current enhancement, the data were again reproducible. The remaining electrodes proved to be acceptable for further investigations. These experimental voltammetric features, then, were sufficient to screen out electrodes whose responses were uncharacteristic of an electrode surface surrounded by an insulator matrix.

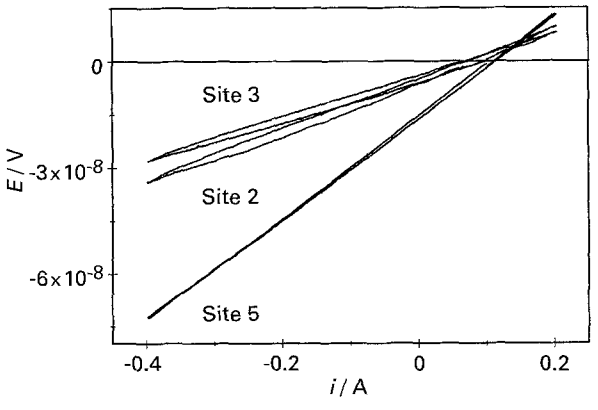

Fig. 3. Voltammograms acquired at 50 mV s^{-1} for the UM CN1 probe 25 electrode in PBS electrolyte for the three sites indicated.

Measurements were made in the phosphate buffered saline supporting electrolyte, to provide data from which apparent capacitance values could be obtained and to allow background corrections to be made to the voltammograms acquired in the presence of the depolarizer. Two important facts emerged from these background voltammograms. For all electrodes examined, the background currents were substantially larger than those predicted from the electrodes' geometric areas. At high scan rates, the measured currents were often comparable in magnitude to the faradaic currents in the presence of the depolarizer. All sites on UM CN1, and the Microprobe 10–2 and 20–2, the background currents showed significant *asymmetry*, Fig. 3.

3.2. *Single cycle voltammetric measurements for HMRI, MP, UM electrodes*

Mathematical models are not available to describe the electrochemical responses acquired with ultramicroelectrodes of the *specific* geometries studied here. If such theories were available, it is unlikely that the solutions would be in analytical form, and thus

simplifications would be necessary to accomplish numerical solutions. It is reasonable then to characterize the present electrodes, using existing models for the conventional disc, hemisphere, and cylindrical geometries, recognizing the approximations that this entails [25].

For electrodes of the dimensions studied here, it is anticipated that at scan rates below $0.05\,V\,s^{-1}$, steady state or pseudo steady state currents would be obtained from which a characteristic dimension for each electrode can be derived. On the other hand, for the UM and the large HMRI electrode, if voltammograms are acquired at scan rates above $\sim 20\,V\,s^{-1}$, the area of the electrode can be evaluated from the Randles Sevcik equation. In the case of the microprobe electrodes, semiinfinite linear diffusion conditions can be expected only at scan rates above $1\,kV\,s^{-1}$. Voltammetric data were acquired for all the ultramicroelectrodes in the scan rate range 0.01 to $100\,V\,s^{-1}$. Inspection of the diagnostic attributes extracted from the voltammograms showed that each electrode type had unique characteristics which were scan rate and geometry dependent. These results are now presented.

UM electrodes probe 23 SX-01. Voltammograms were obtained for each of the five iridium electrode sites. The highest value of the current was measured with site 5 and the lowest with site 3. The sites 1, 2, 4 and 5 gave voltammograms whose characteristics are similar. For site 3, the voltammograms are substantially different. Data for site 5, representative of the concurring electrode sites will be described, followed by the data representing site 3. A comparison of the voltammograms acquired at sites 3 and 5, at different scan rates, is made in Figs 4 and 5.

Probe 23, site 5. Single cycle voltammograms corrected for background currents are wave shaped at the scan rates 0.010 and $0.020\,V\,s^{-1}$. The forward and the backward curves coincided in the plateau region but the cathodic and anodic branches are separate in the rising portion of the voltammograms. The plateau current is independent of the scan rate. These results are consistent with sites that

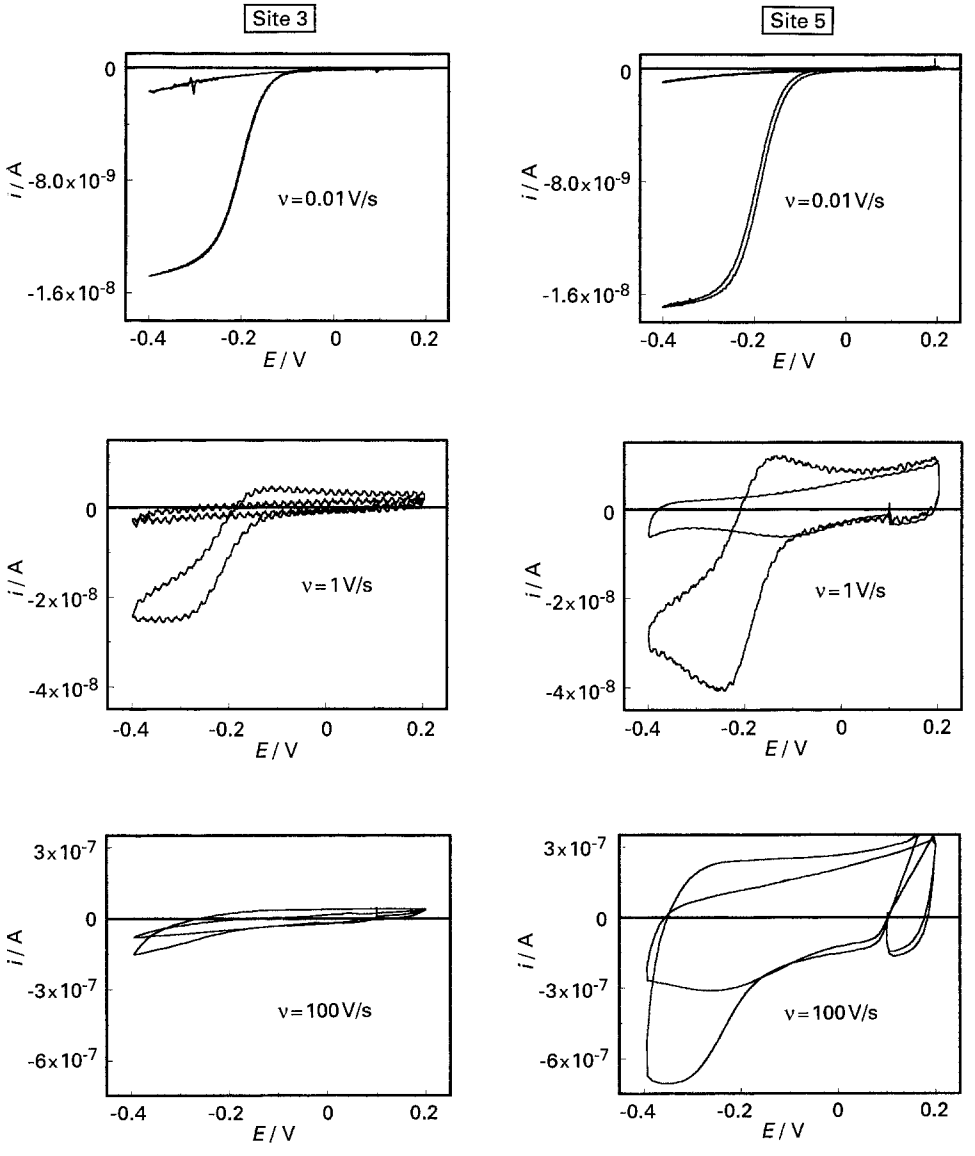

Fig. 4. The influence of the scan rate on the voltammetric responses acquired for the UM SX-01 probe 23 on sites 3 and 5 both in a solution 3.3 mM in $Ru(NH_3)_6Cl_3$ in PBS and in the supporting electrolyte alone.

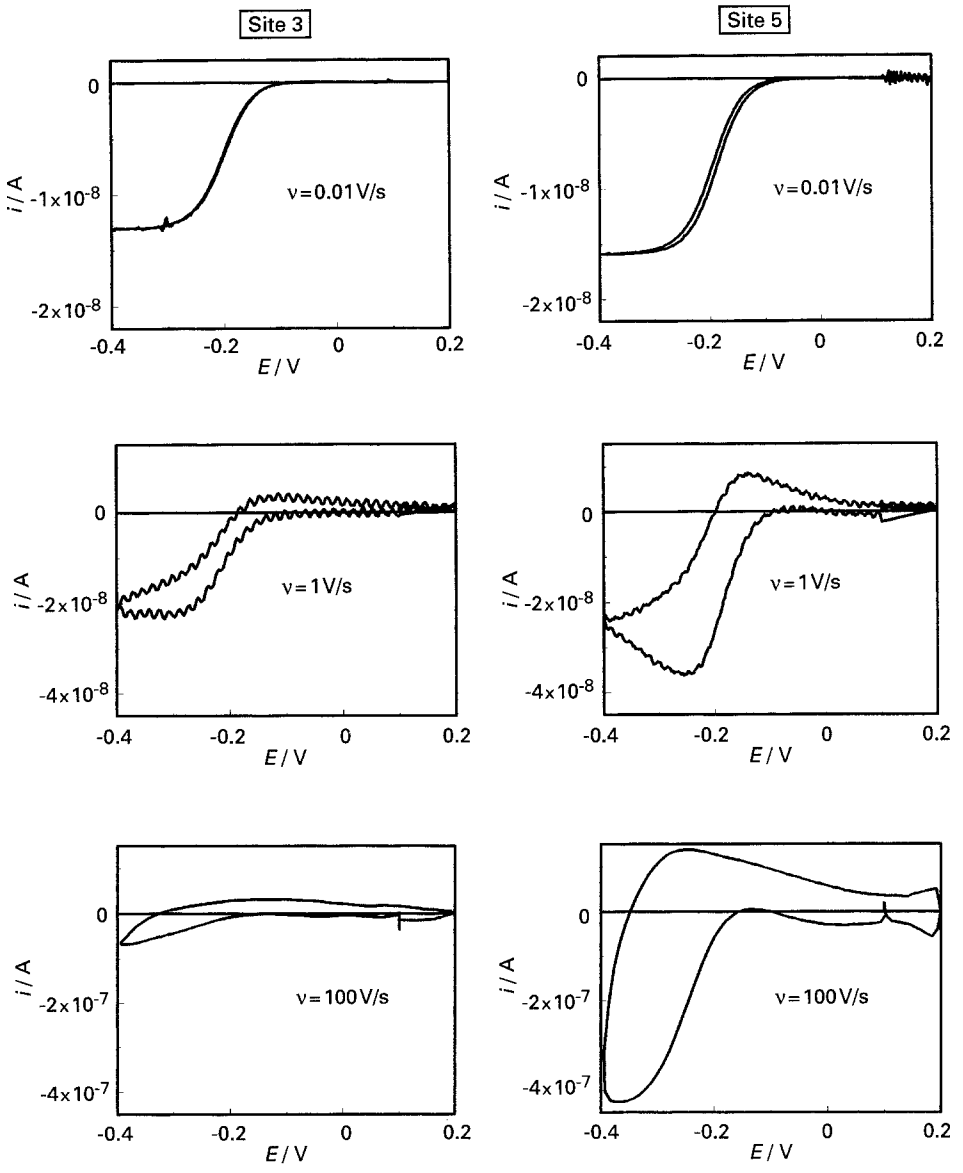

Fig. 5. Background corrected voltammograms, (corresponding to those in Fig. 4) acquired for the UM SX-01 probe 23 electrode, sites 3 and 5 in a solution 3.3 mM in $Ru(NH_3)_6Cl_3$ in PBS.

behave like a disc electrode to which mass transport is under nonlinear diffusion control. Distinctive cathodic and corresponding anodic peaks are observed at scan rates between 0.050 and 5.0 V s^{-1}. For this scan rate range, the absolute values of the current function, $i_p/\nu^{1/2}$, for the forward peak decrease as the scan rate increases. Although the peak potential and the half-peak potential are

Table 2. Cyclic voltammetric data for the reduction process at the UM SX-01 probe 23, site 5 electrode in the solution of 3.3 mM $Ru(NH_3)_6Cl_3$ in PBS buffer solution

$\nu/V\,s^{-1}$	$^cE_p/V$	$^aE_p/V$	$^cE_{p/2}/V$	$-i_p/nA$	$-i_p/\nu^{1/2}/nA\,V^{-1/2}\,s^{1/2}$	$r_d/\mu m$
0.0100	—	—	−0.190	16.0	160	18.3
0.0200	—	—	−0.188	16.0	113	17.8
0.0500	−0.290	−0.100	−0.185	17.4	77.8	18.0
0.100	−0.270	−0.110	−0.182	18.4	58.2	17.7
0.200	−0.255	−0.130	−0.182	21.0	47.0	17.9
0.500	−0.250	−0.140	−0.182	27.2	38.5	18.4
1.00	−0.255	−0.140	−0.182	34.8	34.8	18.7
2.00	−0.270	−0.140	−0.190	45.0	31.8	18.8
5.00	−0.280	−0.140	−0.200	67.5	30.2	19.2

Data obtained from the cyclic voltammograms corrected for the charging and residual current.
Electrode radius, r_d, calculated using the experimental data and the Aoki [7] equation (1) for maximum current at the disc electrode.
Potential against Ag|AgCl|3 M NaCl|| reference electrode.

cathodic with respect to the values for linear diffusion conditions and initially shift anodically, at the higher scan rates, a reversal of this trend takes place which is more marked for the E_p than the $E_{p/2}$ values. The peak widths are wider and the separation of the peaks are significantly larger than those for linear diffusion conditions. The numerical data for the electrodes are collected in Table 2. The characteristics of the potential data suggest the involvement of *iR* contributions that arise from the nature of the iridium film, *vide infra*. For scan rates above $5\,V\,s^{-1}$, the background currents at potentials before the wave, Fig. 4 are larger than those obtained in the presence of the depolarizer. Thus the background subtraction process over corrects voltammograms for the depolarizer and valid diagnostic quantities can not be obtained. The sequence of measurements was depolarizer, supporting electrolyte. To examine the question of an enhancement in the background, the electrode was reintroduced into the depolarizer solution and voltammograms recorded. There is no measurable difference between the original data and those obtained after the background measurements. The reason for the enhancement of background currents or the depression of the currents in the presence of the depolarizer is not clear at this time.

Probe 23, site 3. Single cycle voltammograms are wave shaped at scan rate between 10 to $50\,mV\,s^{-1}$. The forward and the reverse currents separate in the rising portion of the voltammogram as the scan rate increases. However, peaks never develop, instead, the voltammograms remain wave shaped for the entire scan rate range explored up to $100\,V\,s^{-1}$, see Fig. 5.

In the scan rate range, 0.01 to $0.5\,V\,s^{-1}$, the half-maximum potentials, ${}^cE_{m/2}$, are up to 0.040 V cathodic with respect to the value measured under linear diffusion conditions, Table 1. ${}^cE_{m/2}$ shifts even more cathodically for scan rates above $0.5\,V\,s^{-1}$. Besides these cathodic shifts of the wave position, the current never reaches a true plateau, but continuously increases with potential for scan rates above $5\,V\,s^{-1}$. Thus, in this scan rate range, the maximum current and consequently ${}^cE_{m/2}$, can not be measured precisely. From the measured plateau currents for the scan rate range 0.01 to $5\,V\,s^{-1}$, the absolute values of the current function decrease as the scan rate is increased, see Table 3.

The five octagonal sites of SX-01 probe 23 had a geometric length and width of 52.4 and 18.2 μm, respectively, corresponding to an area of 1000 μm^2. Assuming that such an area can be represented by an equivalent disc, then the disc radius is $r_d = 17.7\,\mu m$ If it is inferred that the electrode sites 1, 2, 4 and 5 are of such a geometry, the corresponding voltammograms can be analyzed with the equation appropriate for the disc current. The following equation, developed by Aoki [7], to express the maximum and/or the peak currents:

$$(i_p/4C_0^b)(\nu/nFRTD_0^3)^{1/2} = 0.34p\exp(-0.66p) + 0.66p - 0.13p\exp(-11/p) + 0.35p^2 \quad (1)$$

can be used to calculate the radius of the disc, in view of the following definition of p:

$$p = r_d\left(\frac{nF\nu}{D_0RT}\right)^{1/2} \quad (2)$$

Values of the radius, obtained at each scan rate, are listed in Tables 2 and 3 for sites 5 and 3, respectively. The value of the radius, $(17 \pm 2)\,\mu m$, is obtained if the mean of the mean values of the radii for sites 1, 2, 4 and 5 is calculated as the 95% confidence level. The area calculated from this datum is $(900 \pm 200)\,\mu m^2$ which is in good agreement with the design goal of 1000 μm^2 for each site. However, at scan rates above $0.2\,V\,s^{-1}$ a dependence of the values of the radii on scan rate and the general distortion of the voltammograms acquired above $5\,V\,s^{-1}$ indicated the porous nature of the sputtered iridium metal, *vide infra*.

HMRI electrodes. Large electrode. Representative voltammograms are shown in Fig. 6 and the diagnostic data are collected in Table 4. Cursory inspection of the shapes of the voltammograms suggest that the responses comply with those expected for a disc electrode. For example, at the lowest scan rates ($0.010–0.020\,V\,s^{-1}$), the current voltage curves are sigmoidal in shape and the maximum current is independent of scan rate. In addition, the forward

Table 3. Cyclic voltammetric data for the reduction process at the UM SX-01 probe 23, site 3 electrode in the solution of 3.3 mM $Ru(NH_3)_6Cl_3$ in PBS buffer solution

$\nu/V\,s^{-1}$	${}^cE_{p/2}/V$	$-i_m/nA$	$-i_m/\nu^{1/2}/nA\,V^{-1/2}\,s^{1/2}$	$r_d/\mu m$
0.0100	−0.205	13.0	130	15.1
0.0200	−0.210	12.8	90.2	14.5
0.0500	−0.210	13.1	58.7	14.2
0.100	−0.208	14.8	46.6	14.8
0.200	−0.208	16.2	36.2	14.8
0.500	−0.210	19.0	26.8	14.5
1.00	−0.212	22.0	22.0	14.1
2.00	−0.220	27.0	19.1	14.0
5.00	−0.225	36.0	16.1	13.6

Data obtained from the cyclic voltammograms corrected for the charging and residual current.
Electrode radius, r_d, calculated using the experimental data and Aoki [7] Equation (1) for the maximum current for disc electrode.
Potential against Ag|AgCl|3 M NaCl|| reference electrode.

Table 4. Cyclic voltammetric data for the reduction process at the HMRI-IC-06-02 electrode in the solution of 3.3 mM $Ru(NH_3)_6Cl_3$ in PBS buffer solution

$\nu/V\,s^{-1}$	${}^cE_p/V$	${}^aE_p/V$	${}^cE_{p/2}/V$	$-i_p/nA$	$-i_p/\nu^{1/2}/nA\,V^{-1/2}\,s^{1/2}$
0.0100	—	—	−0.195	11.6	116
0.0200	—	—	−0.195	11.6	82.0
0.0500	—	—	−0.190	12.2	54.6
0.100	—	—	−0.185	12.2	38.9
0.500	−0.260	−0.125	−0.180	14.5	20.5
1.00	−0.255	−0.130	−0.180	17.2	17.2
2.00	−0.250	−0.140	−0.180	21.5	15.2
5.00	−0.265	−0.150	−0.185	31.5	14.1
10.0	−0.270	−0.160	−0.185	43.0	13.6
20.0	−0.275	−0.160	−0.190	68.0	15.2
50.0	−0.290	−0.130	−0.215	121.0	17.1
100	−0.325	−0.145	−0.220	190.0	19.0

Data obtained from the cyclic voltammograms corrected for the charging and residual current.
Potential against Ag|AgCl|3 M NaCl|| reference electrode.

and reverse currents are almost superimposed. At higher scan rates ($> 0.5\,V\,s^{-1}$), the voltammograms are peak shaped. The peak position shifts anodic with respect to the position of the steady state wave. The characteristics of these peaks approach those expected for semi infinite linear diffusion. These results, then, appear to be consistent with those expected for an embedded disc electrode [7]. However, a more detailed consideration of the diagnostic criteria suggest that the data do NOT comply

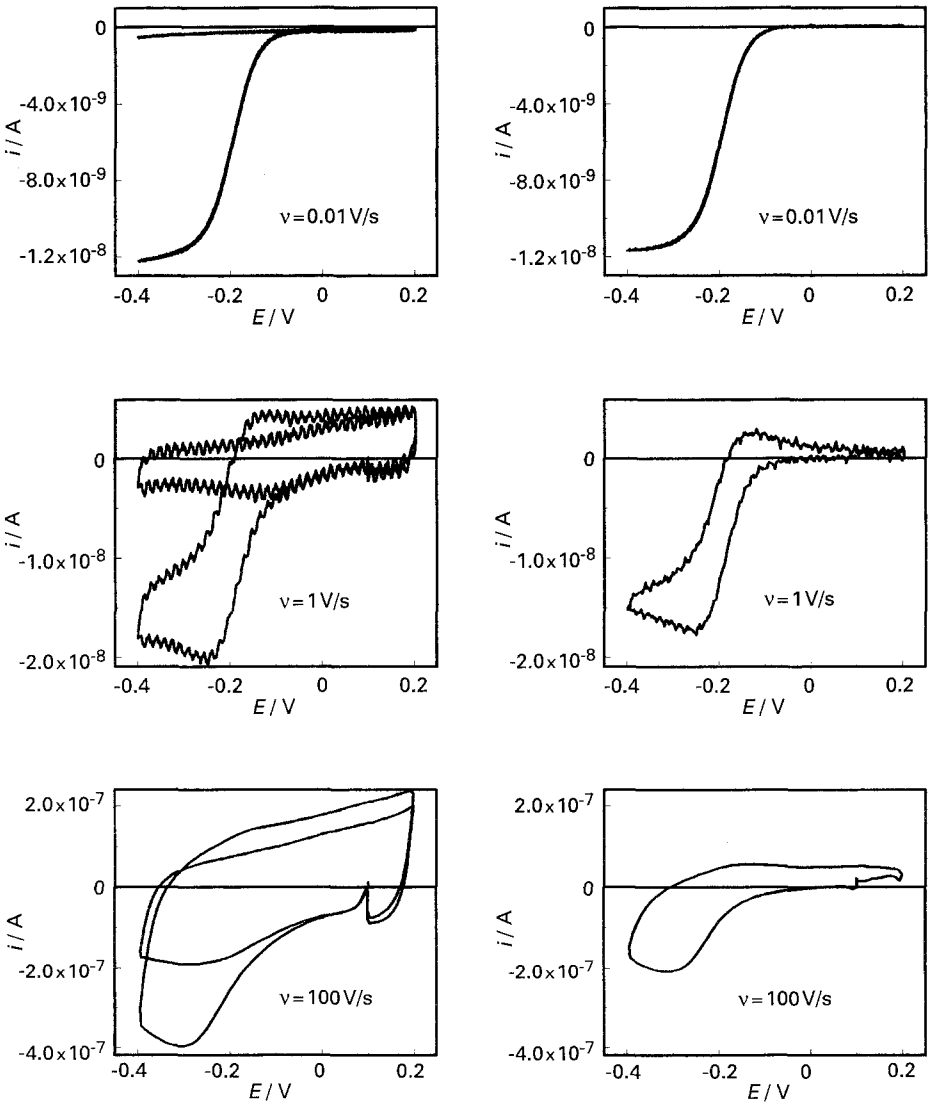

Fig. 6. Representative voltammograms for the HMRI-IC-06-02 electrode acquired in a solution 3.3 mM in $Ru(NH_3)_6Cl_3$ in PBS and in the background electrolyte, left side of the figure. The voltammograms shown on the right side are corrected for the charging and residual currents.

completely with those expected for a disc electrode over the experimental range of scan rates used. Particularly, the current function, $i_p/\nu^{1/2}$, decreases as the scan rate increases to reach a minimum at around $10\,V\,s^{-1}$, then increases again as the scan rate continues to increase. For a disc electrode, the value of $i_p/\nu^{1/2}$, is expected to reach a limiting value corresponding to that expected for semiinfinite linear diffusion.

Small electrode. At low scan rates, 0.010 to $0.020\,V\,s^{-1}$, the voltammograms have a sigmoidal shape, in which the forward and the reverse curves are almost coincident and the maximum currents are independent of the scan rate. A separation of the forward and reverse curves occurs as the scan rate increases. However, a peak did *not* appear in the potential window used and the voltammograms continued to exhibit a sigmoidal shape. The half-maximum potential is more cathodic in comparison to that for the bigger electrode. When the background current subtraction was applied, Fig. 7, the resultant voltammogram showed a loop over in the current that occurs because, at a given potential, the forward current is less cathodic than the reverse current! Above $0.5\,V\,s^{-1}$, numerical diagnostic quantities can not be obtained from such distorted voltammograms, Fig. 7.

The cathodic displacement of the steady-state voltammograms for the smaller electrode in comparison to the larger electrode can not be explained by an uncompensated resistance contribution. Under diffusion controlled conditions, Oldham [26] demonstrated that the magnitude of the uncompensated resistance for the 'true steady-state' is independent of the size and shape of the ultramicroelectrode. This point is taken up later.

At $0.01\,V\,s^{-1}$ the limiting steady state currents for the two electrodes are $i_L = 11.6$ and 2 nA, respectively. These currents are not in the ratio expected from the electrode's geometric surface

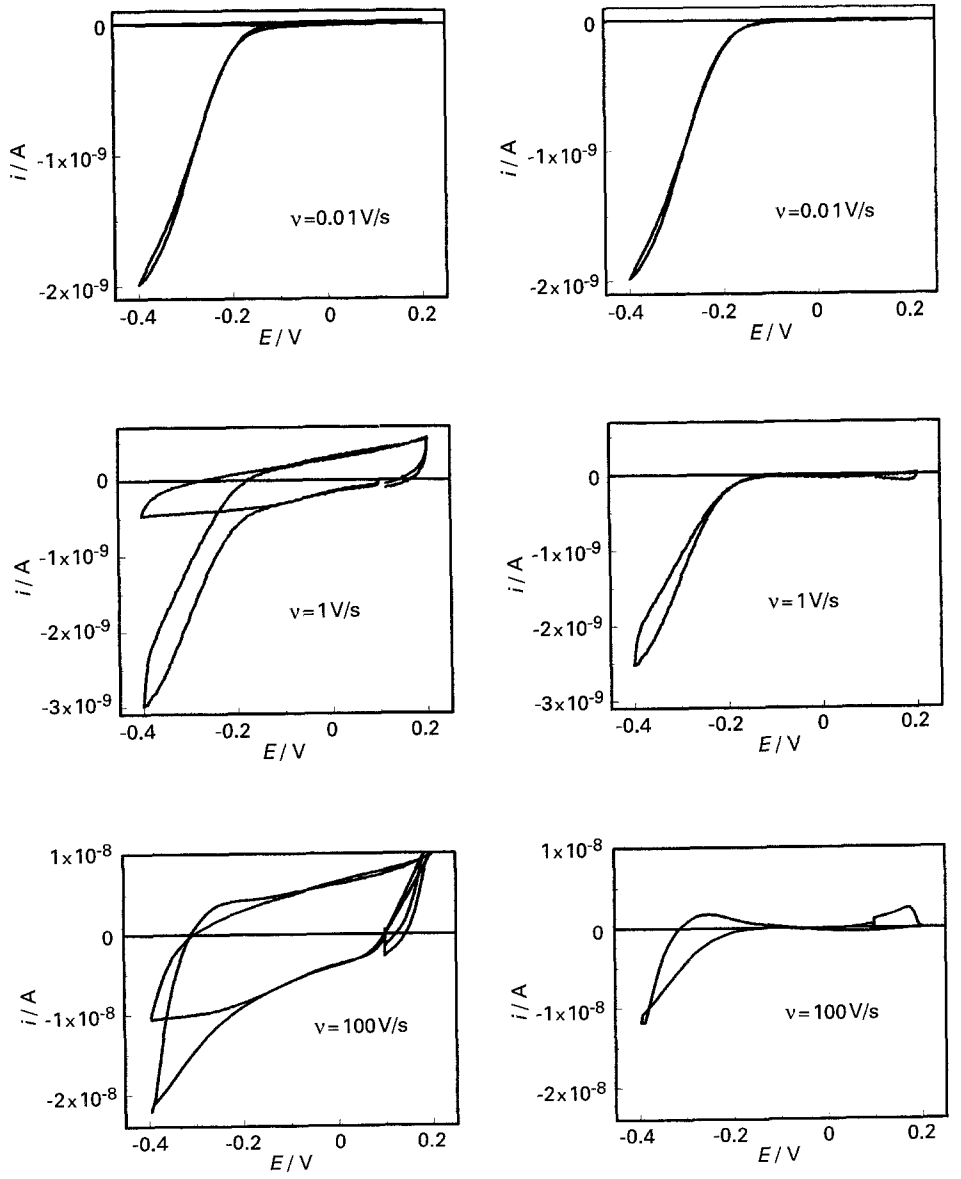

Fig. 7. Representative voltammograms for the HMRI-IC-05-06 electrode acquired in a solution 3.3 mM in $Ru(NH_3)_6Cl_3$ in PBS and in the background electrolyte, left side of the figure. The voltammograms shown on the right side are corrected for the charging and residual currents.

Table 5. Optically and electrochemically determined dimensions of Microprobe electrodes

Electrode identity	Design length/μm	Optically determined			Electrochemically determined
		Length, b/μm	Radius, r/μm	Area, A/10^6 cm^2	Altitude, h/μm
10–1	10	9	1.9	0.54	9
10–3	10	6	1.3	0.35	15
20–1	20	22	3.4	2.5	34
20–3	20	20	2.5	1.9	62

Area calculated for a cone.

areas. The electrochemical radius, r_d, for each electrode was calculated from these values, and the expression for the limiting current for an ultramicrodisc electrode [27–29]:

$$i_{ss} = 4nFC_0^b D_0 r_d \quad (3)$$

The values of the radii for large and small electrodes are 14 and 2.7 μm, respectively. As the scan rate was increased, only the voltammograms for the larger electrode became peak-shaped, Fig. 6. The dimensionless quantity, p, was obtained for each scan rate from the maximum current, i_p, by solving the Aoki equation (1). The radius, calculated from the average value of p for the first three scan rates is 13 ± 1 μm from which the area is (530 ± 80) μm^2. At higher scan rates, the distinct trends in the data with scan rate make the evaluation of p and hence, r, from the Aoki equation and the area, A, from the Randles' equation from the peak current, unwise.

Microprobe electrode. Optical microscopy confirmed that these electrodes were nominally cone shaped. The dimensions of the electrodes were measured from photographs at 400× magnification with an error of about 10% and are included in Table 5. It may be postulated that, for electrodes with these geometric dimensions, the single cycle voltammograms will approximate those obtained at a hemispherical ultramicroelectrode [30]. Results are presented to explore this premise for a representative electrode (10–1) of this set.

At the lowest scan rates, the voltammograms are wave shaped, but the forward and the reverse currents *do not* coincide. The condition for the observation of a steady state current, to better than 2%, is given by:

$$\nu d^2 \ll \frac{DRT}{400nF} \quad (4)$$

From the geometric dimension of the wire, the superficial diameter, d, for the cone is between 18 and 63 μm, and the true steady-state voltammogram will be obtained only at scan rates lower than 0.13 and 0.01 mV s^{-1}, respectively [31]. Interference due to convection is appreciable at these scan rates. It was suggested [32], based on experimental data, that voltammograms for the hemisphere remain virtually constant when the scan rate significantly exceeds the value predicted by Oldham's criteria.

A distinct cathodic peak and a corresponding anodic peak are observed for scan rates higher than 0.050 V s^{-1}. Above 1 V s^{-1}, the voltammetric shape becomes more symmetrical than that expected for linear diffusion conditions, see Fig. 8. The numerical values of the voltammetric diagnostic quantities are complex functions of the scan rate which do not comply with the diagnostic criteria for the hemispherical electrode, Table 6. The characteristics of these diagnostic criteria for this electrode as a function of scan rate are summarized as follows (see also Table 1):

(i) The current function, $i_p/\nu^{1/2}$, decreases as the scan rate increases but reaches a minimum at about 0.2 to 0.5 V s^{-1}. On raising the scan rate beyond these values, $i_p/\nu^{1/2}$, increases. For a hemisphere, the value of $i_p/\nu^{1/2}$, is expected to reach a limiting value, of 0.81 nA V$^{-1/2}$ s$^{1/2}$, corresponding to that expected for semiinfinite linear diffusion and the electrolyte conditions used.

(ii) The forward cathodic peak becomes well defined at 0.050 V s^{-1}. An increase in the scan rate results in an anodic shift of the peak potential that reaches a value of $^cE_p = -0.212$ V, at between 0.5 and 1 V s^{-1}. This value is more *anodic* than expected for linear diffusion conditions. Further increases in the scan rate cause ^cE_p to shift cathodically.

(iii) The half-peak potential, $^cE_{p/2}$ or $^cE_{m/2}$ shifts anodically with increasing scan rate, but becomes constant in the range 0.5–2 V s^{-1} where the value of $^cE_{p/2}$ is -0.155 V. This value is slightly *anodic* of that obtained for other microelectrodes for this system. On further increases in the scan rate, $^cE_{p/2}$ shifts back in a cathodic direction.

(iv) The peaks separation, $^aE_p - {}^cE_p$, decreases as the scan rate increases, reaching a minimum value of about 0.045 V in the range 0.5–2 V s^{-1}. This value is smaller than that observed under linear diffusion conditions. Further increases in the scan rate result in an increase of this separation of the peaks.

(v) The half-peak width, $^cE_{p/2} - {}^cE_p$, decreases as the scan rate increases, reaching a minimum value of 0.057 V between 0.5–1 V s^{-1} which is close to the value expected under linear diffusion conditions. Further increases in the scan rate causes an increase in the half peak width.

The voltammograms acquired at electrodes 10–3, 20–1 and 20–3, have characteristics similar to those presented for electrode 10–1. The trend of the voltammetric diagnostic quantities for all these electrodes in the scan rate range, 0.01 to 0.2 V s^{-1} are consistent

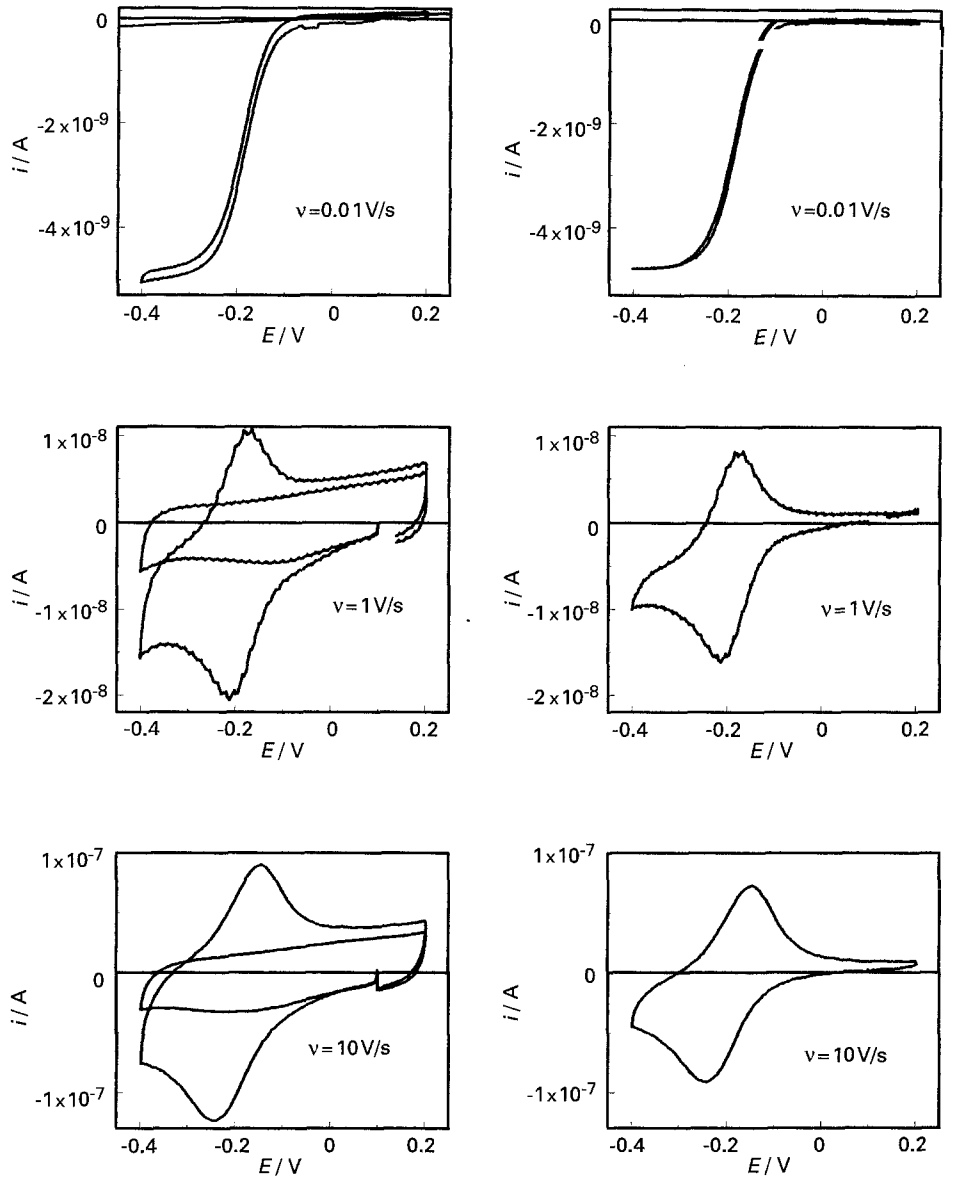

Fig. 8. Voltammograms acquired for Microprobe electrode, 10–1, in a 1.96 mM of $Ru(NH_3)_6Cl_3$ in PBS and in the background electrolyte identifying a contribution due to restricted diffusion, to the total current at intermediate scan rates. Right side figures show the background corrected voltammograms.

Table 6. Cyclic voltammetric data for the reduction process at the Microprobe electrode, 10–1, in the solution of 1.96 mM $Ru(NH_3)_6Cl_3$ in PBS buffer solution

$\nu/V/s$	$^cE_p/V$	$^aE_p/V$	$^cE_{p/2}/V$	$^cE_{p/2} - ^cE_p/V$	$-i_p/nA$	$-i_p\nu^{-1/2}/nA\,V^{-1/2}\,s^{1/2}$
0.0100			−0.184		4.78	47.8
0.0200			−0.180		4.70	33.2
0.0500					5.60	25.0
0.0500			−0.178		5.10	22.8
0.100	−0.253	−0.106	−0.169	0.084	5.55	17.6
0.200	−0.235	−0.135	−0.165	0.070	5.80	13.0
0.200	−0.23	−0.15	−0.168	0.062	6.14	13.7
0.500	−0.215	−0.17			9.25	13.1
0.500	−0.212	−0.17	−0.155	0.057	9.80	13.9
1.00	−0.212	−0.14	−0.155	0.057	16.0	16.0
2.00	−0.215	−0.17	−0.155	0.060	27.5	19.5
5.00	−0.237	−0.16	−0.166	0.071	53.0	23.7
10.0	−0.243	−0.148	−0.17	0.073	90.4	28.6
20.0	−0.27	−0.129	−0.181	0.089	143	31.9
50.0	−0.335	−0.058	−0.208	0.127	248	35.0
100	−0.4	−0.057	−0.252	0.148	360	36.0

Data obtained from the cyclic voltammograms corrected for the charging and residual current.
Potential against Ag|AgCl|3 M NaCl|| reference electrode.

with a faradaic process occurring under nonlinear diffusion conditions. The theory predicts, however, that at higher values of the scan rate, the diagnostic quantities will gradually change to those expected for linear diffusion conditions. The diagnostic quantities for ${}^{c}E_{p}$ and ${}^{c}E_{p/2}$ show the presence of extrema whose values are 0.018 and 0.015 V anodic of the values obtained under linear diffusion conditions, Table 1. Importantly, it is also noted that the voltammetric shape becomes symmetrical at higher scan rates that indicates a contribution from restricted diffusional mass transport. This provided a *key factor* in the development of the subsequent model to explain and quantify the data from these electrodes and those from HMRI.

The steady state currents observed for the four Microprobe electrodes were not fully compliant with true hemispherical diffusion. However, by applying the concept of superficial diameters [27], a number was obtained that was related directly to the principle dimensions of a cone and from which the altitude, h, could be calculated when the basal radius, r_c is known from microscopical measurement. From Oldham's definition, and the steady state current at a hemisphere, the corresponding current at a cone shaped electrode is

$$i_{ss} = 4\sqrt{(h^2 + r_c^2)}nFC_0^b D_0 \qquad (5)$$

From the maximum current data for each electrode at 0.01 and 0.02 V s^{-1}, this equation was used to calculate $\sqrt{(h^2 + r_c^2)}$. The altitude, h, was evaluated. These data are compared with the microscopically determined values of h in Table 5. While the two independently determined values of h, for the Microprobe 10–1 electrode were in good agreement, the electrochemically determined values of h for the other three electrodes were much larger than those determined microscopically. These differences are interpreted by the loss of continuity between the insulator and the iridium wire that results in a peeling back of the insulator to form a 'petal-like' structure not easily distinguishable under the microscope.

3.3. *Apparent capacitances at all electrodes*

The apparent capacitance was determined from the background current, i_r, measured at 0.000 V against the silver–silver chloride reference electrode, and the experimental scan rate, for the scan rate range 0.01 to 200 V s^{-1}. The apparent capacitances, normalized to the geometric area, decrease as the scan rate is increased, for all electrodes examined (see Fig. 9). The dependence of the apparent capacitance on scan rate is different for each electrode design and at least

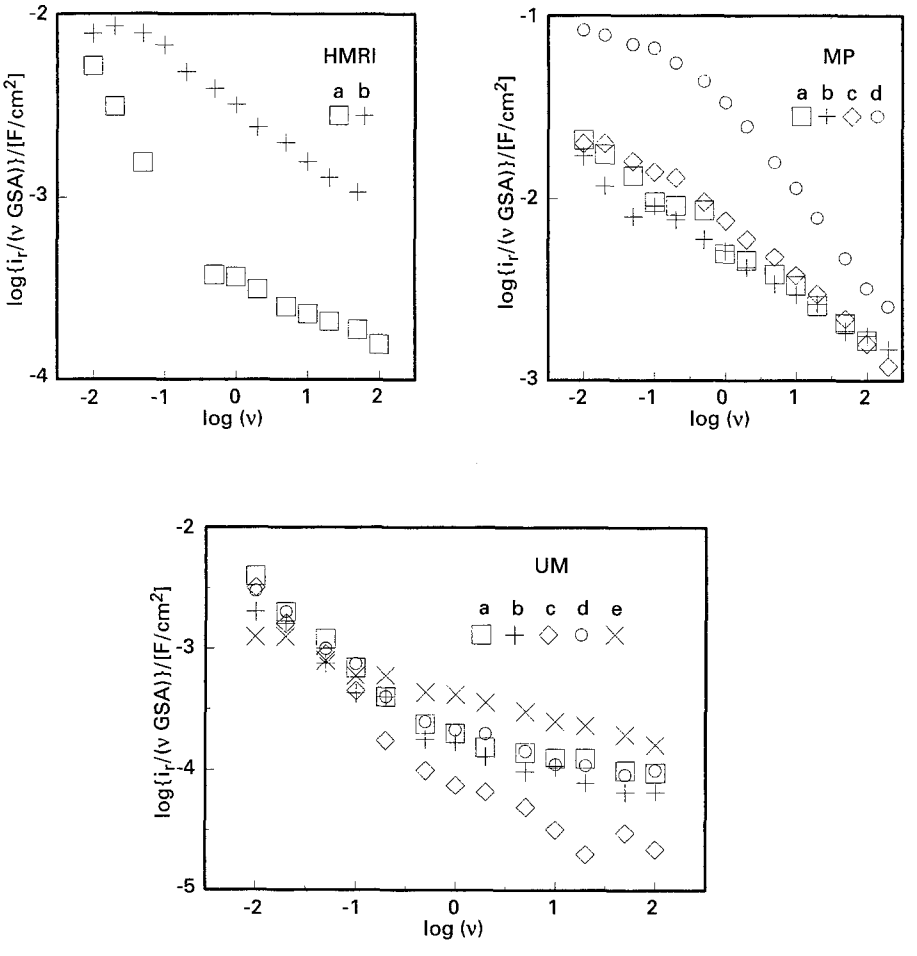

Fig. 9. The relationship between the normalized apparent capacitances, C_d/A_{GSA} and the scan rate for: HMRI (a) IC-06-02 and (b) IC-05-06; MP (a) 10–1, (b) 10–3, (c) 20–1 and (d) 20–3; UM SX-01 probe 23 sites; (a) 1, (b) 2, (c) 3, (d) 4 (e) 5.

four reasons may be advanced to explain this behaviour:

(a) The measured residual current includes contributions from both charging and faradaic currents due to impurities.
(b) The presence of the uncontrolled amounts of iridium 'oxide' materials on the electrode.
(c) The formation of porous, rather than dense, iridium films during sputtering.
(d) The supporting electrolyte infiltrates between the metal and the insulator layers.

The presence of impurities can be excluded because the same electrolyte solutions were shown to be free of impurities by measurements with a BAS microelectrode. Conway [13] showed that the redox processes associated with bulk iridium oxide film becomes irreversible above $5\,V\,s^{-1}$. If the scan rate dependences of the measured apparent capacitances result from contributions by cathodic faradaic processes involving the surface IrO_x, then the capacitance data would show a complex dependence on scan rate. For an irreversible surface process, the theory predicts that the logarithm of the current density varies with the scan rate according to the relationship:

$$\ln\left(\frac{i}{A}\right) = \ln(nFkC) - \frac{\alpha n_\alpha F}{RT}(E - E^{0\prime}) - \frac{RTk}{\alpha n_\alpha F f_{th} \nu} \times \exp\left[\frac{\alpha n_\alpha F}{RT}(E - E^{0\prime})\right] \quad (6)$$

where, f_{th}, is the thickness of the IrO_x film. The logarithm of the current densities used to calculate the apparent capacitances never showed the linear dependence on the reciprocal of the scan rate required by the above equation for each electrode examined. This contrasted with recent data for sputtered iridium electrodes that showed close agreement with Equation 6 indicating the presence of substantial amounts of iridium oxide formed under these conditions [33]. Thus the possibility that the scan rate dependence of the apparent capacitance is due to faradaic currents arising from a surface process involving IrO_x may be rejected.

In the case of the UM electrode sites, it is likely that the observed responses are dominated by porous iridium produced in the sputtering process. Two pieces of evidence support this proposition.The measured area, A_T, can be expressed in terms of the exposed area, A_{exp}, and the peripheral area, A_p. Using the reported thickness of the sputtered iridium film, $0.3\,\mu m$, and the calculated radius of the site (*vide supra*) of $17\,\mu m$ the peripheral contribution is about 4%. For all electrode sites on the UM 23 SX-01 probe, the apparent capacitances decreased by one to two order of magnitude as the scan rate was increased four orders of magnitude. It must be concluded that the large change in apparent capacitance/area of the UM electrodes arises because the exposed surface itself is porous. For the HMRI electrode, constructed from iridium wire, a decrease in the apparent capacitance was also observed as the scan rate increased. However, in that case the corresponding ESA at $100\,V\,s^{-1}$ was higher than the GSA. For the UM electrodes, the ESA at $100\,V\,s^{-1}$ was larger, comparable, or smaller (site 3) than the geometric surface area, Table 7. These results are explained in terms of electrodes that are comprised of porous iridium material. The variation in the areas reflects the area dependence on the pore sizes and the number of the pores present.

Studies with solutions containing the depolarizer, demonstrate that factor (d) makes a major contribution to the capacitative response of the electrodes fabricated for iridium wire. The apparent capacitances of both HMRI electrodes, normalized to the geometric area, are some two orders of magnitude greater than the specific double layer capacitance, $65\,\mu F\,cm^{-2}$, at this potential for an iridium electrode. At the highest scan rates, there is a substantial difference between the two HMRI electrodes. The area of each electrode calculated from the apparent capacitances are some two or twenty times larger than the geometric area for the bigger and smaller electrode, respectively.

The apparent capacitances, normalized to the geometric area, for the four Microprobe electrodes

Table 7. A comparison of the geometric surface area, GSA, with the electrochemically determined area, ESA: {1} on the basis of the apparent capacitance, i/ν, for the highest scan rate employed using the value of $65\,\mu F\,cm^{-2}$ and {2} from impedance data

Method		{1}	{2}
	10^6 *GSA/cm*^{2}	10^6 *ESA/cm*^{2}	10^6 *ESA/cm*^{2}
HMRI-IC-06-02	4.77	12	—
HMRI-IC-05-06	0.07	1.2	—
UM SX-01 probe 23, site 1	10.00	15	—
UM SX-01 probe 23, site 2	10.00	10	—
UM SX-01 probe 23, site 3	10.00	3.4	—
UM SX-01 probe 23, site 4	10.00	15	—
UM SX-01 probe 23, site 5	10.00	25	—
IR300310A 10–1	0.54	15	2.0
IR300310A 10–3	0.35	8.0	1.6
IR300320A 20–1	2.5	46	3.6
IR300320A 20–3	1.9	75	6.0

at low scan rate ($0.01\,V\,s^{-1}$) are some two hundred to two thousand times larger than the double layer capacitance for an iridium surface. At the highest scan rate used, $100\,V\,s^{-1}$, the measured value of C_{dl} or the calculated area is still twenty to forty times higher than the double layer capacitance or the geometric areas, respectively. The values of the surface areas for the Microprobe electrodes are higher than the surface areas estimated from impedance data provided by Microprobe. The measurement of impedance was carried out at frequency of 1 kHz. Since the apparent capacitances from the sweep experiments are dependent on the scan rate, it is expected that the impedance is also a function of the frequency. The areas are calculated from the data, therefore, by assuming that the impedance is capacitative and that the phase angle is 80° [23]. Table 7 summarizes these results. Variations in the values obtained by different methods may be reconciled by the difference in the frequency used.

Previous workers have discussed the frequency dispersion of apparent capacitance in terms of either *cracks* [34] formed in the insulation material or the poor quality of the seal [19] between the metal and the insulator. Wightman suggested that leakage into cracks at the seal perimeter is significant for an ultramicroelectrode where the perimeter to area ratio is large. The apparent capacitance was represented by an equivalent circuit which differs from that given in reference [35] page 13. Wightman's equivalent circuit was made up of a resistor R_u in series with a second resistor, R_2 which is in parallel with a capacitor, C_d, representing the double layer capacitance of the exposed area. This model is based upon a misunderstanding of the equivalent circuit proposed by Fox [36]. Consequently, the equations presented by Wightman to describe the behaviour under linear sweep conditions are incorrect for the present situation. Posey [37] and later Newman [38, 39] have presented more appropriate models to describe the charging process at 'idealized' one dimensional pores.

3.4. *Modelling of leakage*

For all electrodes examined, it is clear that semiinfinite linear diffusion conditions alone do not govern the total current. An assessment of electrode areas from these data will lead, therefore, to less realistic estimates of the areas. On the other hand, at the lowest scan rates used for the HMRI and UM electrodes, steady state currents were observed which conformed to hemispherical diffusion at a disc. These currents provided information about the dimensions of the electrode. In addition, data in the intermediate scan rate range 0.2 to $5.0\,V\,s^{-1}$ were handled, with the aid of the Aoki expression for the maximum current [7], to obtain further estimates of electrode radii. For the conical electrodes from Microprobe, while apparent steady state currents were observed, full compliance with true hemispherical diffusion was not obtained. Nevertheless, by applying the concept of superficial diameters [27], conical dimensions were obtained and compared with those measured microscopically. Importantly, apparent capacitance data, converted into areas using the double layer capacitance for iridium showed a strong dependence on electrode design and on frequency [37–39] that coincided with the disturbance of semi infinite linear diffusion conditions in the presence of the depolarizer at the higher scan rates.

While the data at low scan rates for the HMRI-IC-06-02 and Microprobe 10–1 electrodes enabled the electrode dimensions to be determined that conform reasonably well with those obtained microscopically and/or were design goals, there are inconsistencies in the data sets as a whole. These suggest that further detail regarding the electrode's structure might be forthcoming from the data at higher scan rates. Specifically, the intermediate to high scan rate data do not conform to the expected semiinfinite linear diffusion model. For the smaller HMRI electrode and the MP 10–3, 20–1, 20–3 electrodes, assuming a diffusion controlled process at low scan rates, the electrochemical dimensions obtained significantly exceed the geometric ones.

In the case of the HMRI elliptical electrodes, while the fabrication methods were the same, a significant difference in their perimeter to area ratios, i.e. 0.16 and $1.34\,\mu m^{-1}$ should be noticed. This discrepancy between the two HMRI electrodes can not be explained, *vide supra*, by the influence of a 'simple' uncompensated resistance, R_u [26]. Nevertheless, as Oldham was careful to point out, this is only true when the supporting electrolyte ions follow the same pathway during migration as the electroactive species follow in diffusing to and from electrode. This condition may not be fulfilled if a thin layer of electrolyte is present between the electrode and insulator, that is, the seal has failed. If the penetration depth, y, parallel to the electrode axis is significant compared to the perimeter, a nonuniform current distribution is induced by the increased resistance axially to the conductor–insulator surfaces. The contribution arising from this non uniform current distribution effect, iR_c, to the total ohmic drop increases as the perimeter to area ratio increases since R_c is a function of $(1/r_d)$ and P/A is also a function of $(1/r_d)$. For *very* small electrodes, this ohmic effect, which is time dependent, may dominate the total response. Thus, the observed cathodic potential displacements and, at the higher scan rates, the distortion of the voltammetric responses themselves, for the smaller HMRI electrode, arise from this effect [40, 41].

Additional support for the failure of the seal between the insulator and the conducting metal with concomitant penetration by the electrolyte comes from the following facts. For the Microprobe 20–2 electrode, the background currents are *asymmetrical*, and similar to those illustrated in Fig. 3. The voltammograms associated with the microprobe 10–1 and 20–3 electrodes, which were reproducible during the

two hour test period, exhibited current during subsequent data acquisition that had increased by a fixed increment. The ensuing data were reproducible. For all the electrodes examined, background currents were substantially larger than those predicted from their geometric areas. These measured currents were often comparable in magnitude to the faradaic currents, at high scan rates. The apparent capacitance, normalized to the *geometric* area, is a complex function of the scan rate, for each electrode examined, see Fig. 9. Symmetry in the voltammetric responses, see Fig. 8, was observed under certain conditions which indicates the effect of the thin layer.

For the larger HMRI electrode and all Microprobe electrodes, conclusive evidence for seal failures and penetration by the electrolyte comes from the accordance of the voltammetric shapes and their diagnostic quantities with those obtained from a simple construct based upon the combination of nonlinear diffusion and finite volume current contributions.

Voltammograms were constructed by summing the currents calculated from the Nicholson and Shain current function [42] for spherical electrodes and currents calculated from the equation given for a thin layer cell, page 410 in [35]:

$$i = nFA_{\text{exp}}C(aD)^{1/2}\chi + nFA_{\text{exp}}CD(1/r)\zeta + \psi(nF)^2\nu VC/RT \qquad (7)$$

Where ψ is given in equation 10.7.16 of [35] and χ is the current function equal to that for linear diffusion conditions, ζ expresses the spherical contribution, A_{exp}, is the surface area of the 'exposed' electrode, V is the volume of the 'cavity', $a = nF\nu/RT$ and the other symbols have their usual meaning. The values $\chi = f(E - E_{1/2})$ and $\zeta = f(E - E_{1/2})$ define the current as a function of potential for a diffusion controlled faradaic process.

For the current contribution due to the thin layer, it was assumed that there is no nonuniformity of the concentration either perpendicular or parallel to the electrode during the total observation time for the scan rates considered. This requires that the following conditions are met. (a) The concentration across the electrolyte layer, perpendicular to the electrode, must be uniform and consequently the width of the cavity must be much smaller than the diffusion layer thickness. This ensures that in the cavity, the diffusional mass transfer perpendicular to the electrode wall is negligible. (b) The uniformity of the concentration, parallel to the electrode surface in the cavity requires that (i) the length of the cavity, y, is so small that the diffusion parallel to the electrode is negligible, and (ii), the thickness of the cavity must be sufficient so that the currents and corresponding potentials are independent of ohmic effects.

Assumptions (a) and (b) are mutually exclusive! In a real voltammogram, if the cavity is thin enough that voltammetric responses are not influenced by diffusion perpendicular to the electrode, then the nonuniform current distribution within the cavity will modify the responses because of the differences in the solution resistances at different points along the electrode surface [40, 41]. For the *experimental* voltammograms, the iR contributions within the cavity would shift the potentials for the maximum current for the process within the finite volume. A quantitative description of these processes can only be obtained through a complete simulation of the leaky electrode. Nevertheless, the simplified approach employed here serves a useful purpose to characterize the problems associated with the present design of stimulation electrodes.

The simulation constructed voltammograms from currents calculated for two spherical electrodes of radius 1 and 10 μm and currents for 'cavity volumes' of $1.257 \times 10^{-8}\,\text{cm}^3$, $1.257 \times 10^{-11}\,\text{cm}^3$ and $9.425 \times 10^{-10}\,\text{cm}^3$. The diffusion coefficient was $6 \times 10^{-6}\,\text{cm}^2\,\text{s}^{-1}$ for the electroactive species, D_{ox} and D_{red}. This latter assumption implies that $E^{0\prime} = E_{1/2}$. Thus, the potentials for the constructed voltammograms are with respect to $E^{0\prime}$, that is, $E - E^{0\prime}$. The results of the calculations are expressed with a new dimensionless current function, $\phi(E - E^{0\prime})$ defined by

$$\phi(E - E^{0\prime}) = \frac{i}{\nu^{1/2}} \frac{(RT)^{1/2}}{(nF)^{3/2}D^{1/2}CA_{\text{exp}}} \qquad (8)$$

By equation (7), this dimensionless current function $\phi(E - E^{0\prime})$ for a spherical electrode with a contribution due to the finite volume is given by

$$\phi(E - E^{0\prime}) = \chi + \zeta Z \frac{1}{r}\nu^{-1/2} + \psi \frac{1}{Z}\frac{V}{A_{\text{exp}}}\nu^{1/2} \qquad (9)$$

where $Z = (RTD/nF)^{1/2}$. Equation 9 shows that the current function, $\phi(E - E^{0\prime})$, depend on scan rate, exposed surface area of the electrode and the volume of the cavity. Voltammograms for the electrode of radius 1 μm and a 'cavity volume', $9.425 \times 10^{-10}\,\text{cm}^3$, at scan rates between 0.01 and $100\,\text{V}\,\text{s}^{-1}$ are illustrated in Fig. 10. The voltammetric diagnostic quantities are compared in Table 8 for the two spherical electrodes with and without contributions from cavities of the different volumes expressed above. The numerical quantities in the table show that the ratio of the exposed surface area to the volume of the cavity determines the relationships between the diagnostic quantities and scan rate. For the two particular electrodes described above, the current function and the potential are independent of the presence of the cavity under steady state conditions. As the scan rate is increased, the half-maximum potential shows some influence due to the presence of the cavity, but the maximum current function reflects only the diffusional processes to the exposed surface electrode. For a constant cavity volume, the voltammograms for the smaller electrode most markedly show the influence of the cavity.

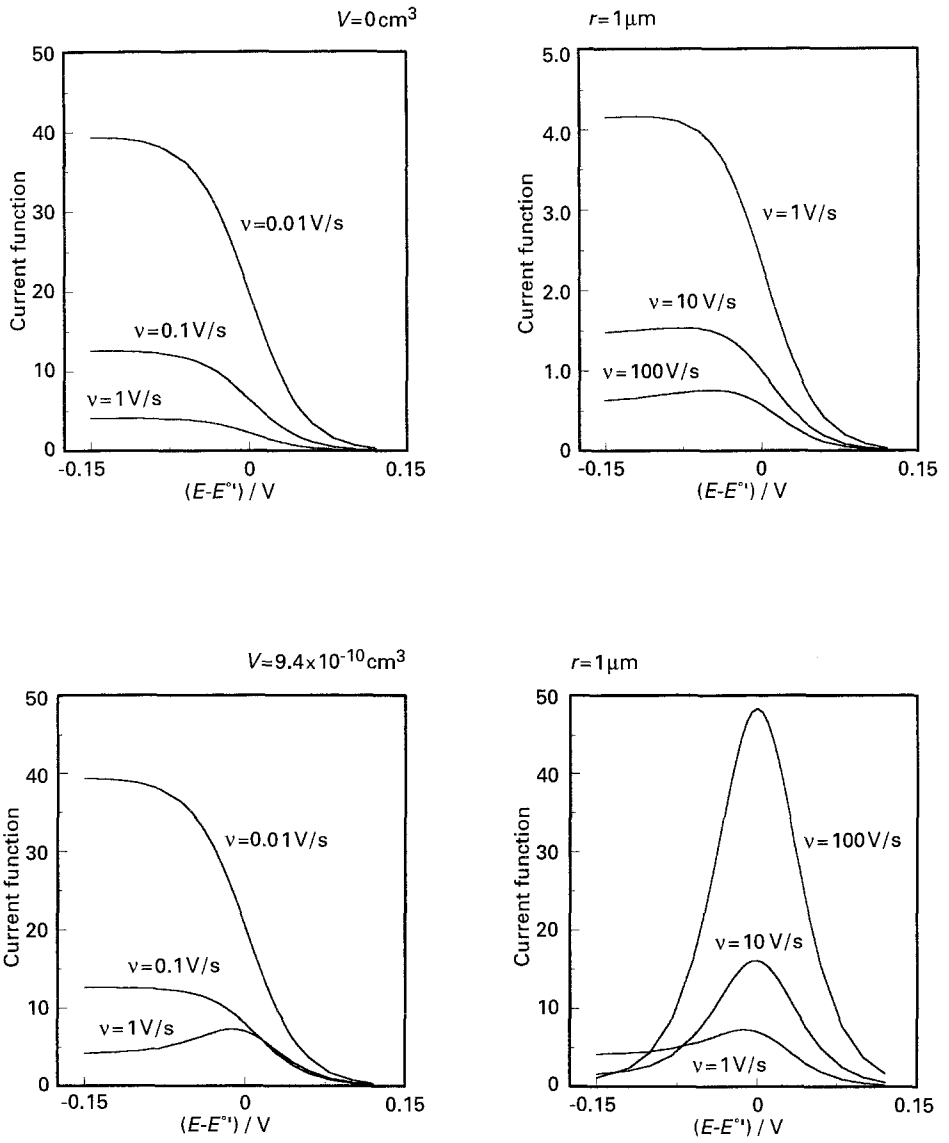

Fig. 10. The influence of the scan rate on the simulated current function for a spherical electrode of 1 μm radius, with and without contributions from the cavity, for the scan rates shown. Volume of the cavity, 9.425×10^{-10} cm^3.

As can be seen from Table 8, the relationship between the maximum current function, ϕ_{max}, and scan rate exhibit a minimum for three of the four conditions considered. Analysis of Equation 9 shows the existence of a minimum. However, the scan rate range in which the minimum is observed depends on the ratio of the exposed surface area to the volume of the cavity and the dimensionality, δ/r, of these electrodes. It can be shown, for example, by consideration of a hemispherical electrode where the perimeter has physical meaning, that the experimental range of scan rates where the minimum is observed, is set by the perimeter to area ratio. Generally, as the perimeter to area ratio increases, the scan rate range in which the minimum is observed, shifts to higher scan rates. Therefore, for experimental voltammograms, the existence of a minimum in the relationship between the maximum current function and scan rate, demonstrates the presence of a cavity.

In principle, to obtain the dimensions of the electrode and the volume of the cavity, the particular values of χ, ζ and ψ for the potential where the maximum occurs should be used in Equation 9. In the voltammogram for a particular electrode, the potential, E_{max}, at which the current function, $\phi(E - E^{0\prime})$, has its maximum value, is itself a function of scan rate. Consequently, the values of χ, ζ and ψ which contribute to the current function, ϕ_{max} at E_{max}, depend on the potential at which this maximum occurs. Therefore, for each scan rate these values of the contributory functions are different. Alternatively, each voltammogram may be deconvoluted to reflect the contributions of the diffusional and finite volume processes. Then the appropriate values for the deconvoluted curves are: $\chi = 0.446$, $\zeta = 0.75$ and $\psi = 0.25$. For real experimental voltammograms, the potential of ϕ_{max} as well as the shape of the voltammograms are most likely influenced by iR, and the exact values of χ, ζ and ψ for the particular potentials are not known, *a priori*.

Without deconvoluted data, a comparison of the actual maximum value, ϕ_{max}, with the sum of the maxima for the contributing functions in the

Table 8. Voltammetric diagnostic quantities from simulated voltammograms for the spherical electrodes with and without contributions from the cavity. Potentials are versus $(E - E^{0\prime})$

Sphere					*Sphere & thin layer*					*Sphere & thin layer*				
$r = 1\,\mu m$					$r = 1\,\mu m$			$V = 1.257 \times 10^{-11}\,cm^3$		$r = 1\,\mu m$			$V = 9.425 \times 10^{-10}\,cm^3$	
ν (V/s)	${}^cE_p$ (V)	${}^cE_{p/2}$ (V)	$\{1\}$	${}^cE_{p/2} - {}^cE_p$ (V)	${}^cE_p$ (V)	${}^cE_{p/2}$ (V)	ϕ_{max}	$\{1\} + \{2\}$	${}^cE_{p/2} - {}^cE_p$ (V)	${}^cE_p$ (V)	${}^cE_{p/2}$ (V)	ϕ_{max}	$\{1\} + \{2\}$	${}^cE_{p/2} - {}^cE_p$ (V)
0.01		0.000	39.1			0.000	39.4	39.1			0.000	39.4	39.6	
0.10		0.000	12.6			0.003	12.6	12.6			0.012	12.6	14.1	
1	−0.12	0.008	4.17	0.128	−0.12	0.008	4.17	4.17	0.128	−0.01	0.038	7.36	8.95	0.048
10	−0.08	0.013	1.54	0.093	−0.06	0.022	1.60	1.74	0.082	0.00	0.042	16.1	16.6	0.042
100	−0.05	0.022	0.764	0.072	−0.01	0.032	1.27	1.40	0.042	0.00	0.046	48.3	48.5	0.046
$r = 10\,\mu m$					$r = 10\,\mu m$			$V = 1.257 \times 10^{-8}\,cm^3$		$r = 10\,\mu m$			$V = 9.425 \times 10^{-10}\,cm^3$	
ν (V/s)	${}^cE_p$ (V)	${}^cE_{p/2}$ (V)	$\{1\}$	${}^cE_{p/2} - {}^cE_p$ (V)	${}^cE_p$ (V)	${}^cE_{p/2}$ (V)	ϕ_{max}	$\{1\} + \{2\}$	${}^cE_{p/2} - {}^cE_p$ (V)	${}^cE_p$ (V)	${}^cE_{p/2}$ (V)	ϕ_{max}	$\{1\} + \{2\}$	${}^cE_{p/2} - {}^cE_p$ (V)
0.01	−0.12	0.008	4.17	0.128	−0.12	0.008	4.17	4.23	0.128	−0.12	0.006	4.17	4.18	0.126
0.1	−0.08	0.013	1.54	0.093	−0.06	0.023	1.60	1.74	0.083	−0.08	0.016	1.54	1.56	0.096
1	−0.05	0.022	0.764	0.072	−0.015	0.037	1.27	1.40	0.052	−0.04	0.026	0.790	0.811	0.066
10	−0.035	0.026	0.542	0.061	−0.005	0.043	2.46	2.56	0.048	−0.02	0.033	0.656	0.693	0.053
100	−0.03	0.028	0.476	0.058	0.000	0.044	6.77	6.86	0.044	−0.01	0.037	0.901	0.953	0.047

$\{1\} = \{\chi + Z\zeta\nu^{-1/2}(1/r)\}_{max}$
$\{2\} = \{(\psi(1/Z)(V/A)\nu^{1/2}\}_{max}$

form $\{0.4463 + [0.75Z\nu^{-1/2}(1/r)]\}$ and $\{0.25(1/Z)(V/A_{exp})\nu^{1/2}\}$, shows that under some conditions the errors in using these values are small (see Table 8). Thus the following approximate equation can be used to determine the electrode dimension, r, and the cavity volume, V.

$$\phi_{max} = 0.4463 + 0.75Z\frac{1}{r}\nu^{-1/2} + 0.25\frac{1}{Z}\frac{V}{A_{exp}}\nu^{1/2} \quad (10)$$

In Table 9, the diagnostic quantities obtained from the voltammograms acquired for the HMRI and Microprobe electrodes are compared with those obtained from simulated voltammograms with and without contributions from the cavity. The diagnostic quantities for the HMRI and Microprobe electrodes are in good agreement with those for the combination of theoretical nonlinear diffusion and the finite volume contributions, bearing in mind the approximations made for the voltammetric constructs. In addition, the relationships between the apparent capacitances and the scan rates, for all electrodes, show that the experimental voltammograms *are* influenced by the nonuniform current distribution associated with such cavities. Therefore, the exact analysis of these data is complex, and for the purposes of the initial evaluation of the fabrication quality, the influence of the nonuniform current distribution can be neglected, bearing in mind the additional need for deconvolution. The application of this general model enables the finite cavity volume and the area of the electrode, accessible to the depolarizer by semiinfinite diffusional mass transport to be evaluated from the dependence of the current function on the scan rate.

The large HMRI electrode was assumed to approximate to a disc. With similar assumptions to those for Equation 10, the Aoki [7] equation (Equation 1) for the maximum current, i_p, at a disc electrode was modified to include a term allowing for the presence of a cavity. The modified equation is

$$(i_p/4C_0^b)(\nu/nFRTD_0^3) = 0.34p\exp(-0.66p) + 0.66p - 0.13p\exp(-11/p) + 0.35p^2 + (nF\nu)^{3/2}V/16(RTD)^{3/2} \quad (11)$$

Based on a series of 'pair-wise solutions' to this expression, the mean radius for the exposed electrode surface and the mean volume of the cavity were obtained as $r = (12 \pm 1)\,\mu m$ and $V = (2.4 \pm 1.2) \times 10^{-10}\,cm^3$.

For the Microprobe electrodes, the electrochemically determined altitudes, h, derived from voltammograms at the lowest scan rates, were larger than those measured microscopically. It is argued that these differences arise from a peeling away of the insulator from the conductor. Consequently, larger lengths of iridium wire were accessible to the electroactive species by semiinfinite diffusion than was

Table 9. Table to compare model diagnostics with diagnostic characteristics obtained experimentally with HMRI and MP electrodes

Electrodes	*Theoretical Spherical*	*Theoretical Spherical & Thin layer*	*HMRI*	*Micro Probe*
$i_p\nu^{-1/2}$ $i_p\nu^{-1/2} = f(\nu)$	> 0.446	> 0.446 "U" shape or	"U" shape	"U" shape
increasing ν	decreasing	decreasing more slowly than spherical		
${}^cE_p = f(\nu)$		anodic shift	anodic shift	anodic shift
increasing ν	shifts anodic	follow by cathodic shift, "U" shape or shifts anodic more slowly than spherical	follow by cathodic shift	follow by cathodic shift
anodic limit of ${}^cE_p$	linear diffusion −0.028 V	thin layer 0 V	more cathodic than linear diffusion	linear diffusion or more anodic
${}^cE_{(m/2)p/2} = f(\nu)$			anodic shift	anodic shift
increasing ν	shifts anodic	shifts anodic faster than for spherical	follow by cathodic shift	follow by cathodic shift
anodic limit of ${}^cE_{(m/2)p/2}$	linear diffusion 0.028 V	thin layer 0.0455 V	slightly cathodic than linear diffusion	more anodic than linear diffusion
${}^cE_{p/2} - {}^cE_p = f(\nu)$		"U" shape	"U" shape	"U" shape
increasing ν	decreases	or decreasing faster than for spherical		
limit of ${}^cE_{p/2} - {}^cE_p$	linear diffusion 0.0565 V	0.042 V < thin layer value of 0.0455 V	≫ linear diffusion	linear diffusion or wider

expected from the original electrode design. Thus, the currents at the exposed area would be better described by a cylindrical model. The Aoki equation for the maximum current at such a cylindrical electrode [43], was modified to include the maximum current due to the finite volume. The equation for the total maximum current-function is

$$i_p/\nu^{1/2} = Z' + Z''\nu^{-0.425} + Z'''(\nu)^{1/2} \qquad (12)$$

Where the coefficients Z', Z'' and Z''' are given by the following equations:

$$Z' = 0.446nFC_0^b\left(\frac{nF}{RT}\right)^{1/2} D_0^{1/2} 2\pi b r_c \qquad (13)$$

$$Z'' = \frac{0.335(nF)^{1.075} C_0^b D^{0.925} 2\pi b r_c^{0.15}}{(RT)^{0.075}} \qquad (14)$$

$$Z''' = \frac{(nF)^2 C_0^b V_{cav}}{4RT} \qquad (15)$$

For the four Microprobe electrodes, a good fit of the experimental data to Equation 12 is obtained. These experimental data and the corresponding function are plotted in Fig. 11. The numerical coefficients for Equation 12 were obtained for each electrode. The radius, the length and the area of the exposed part of the electrode, A_{exp}, as well as the volume of the cavity, V_{cav}, were calculated for each electrode from these coefficients, Table 10.

The electrochemical surface areas of the cavities, A_{cav}, for all electrodes were calculated as the difference between the surface area determined from the corresponding apparent capacitance at the highest scan rate and the exposed area, A_{exp}, determined from the faradaic process. Thus, from this area, A_{cav}, and the volume of the cavity, the width, λ, and the depth, y, of the cavity are obtained. The data are presented in Table 11. For the larger HMRI electrode, the exposed area is equal to the GSA. The area of the metal within the cavity is about one and a half times the GSA. Since the width, λ, of the cavity is less than 3% of the radius, it may be assumed that the diffusional profiles are not strongly influenced by the cavity especially under steady state conditions where the diffusion layer thickness, $\delta = 0.25\pi r_d$, will be about 9.4 μm.

The electrochemical data obtained for the four well behaved Microprobe electrodes are compared with microscopic and nominal dimensions in Table 11. The radii obtained from the electrochemical and microscopic data suggest that the shaft radius is between 1 and 2 μm. The measured and nominal tip lengths are in agreement for the two types of electrode. However, the electrochemical lengths, b, (from Equation 12) are considerably longer than either the nominal or optically measured values. The exposed areas of the four Microprobe electrodes, determined electrochemically from Z' directly, are as much as nine times greater than the calculated

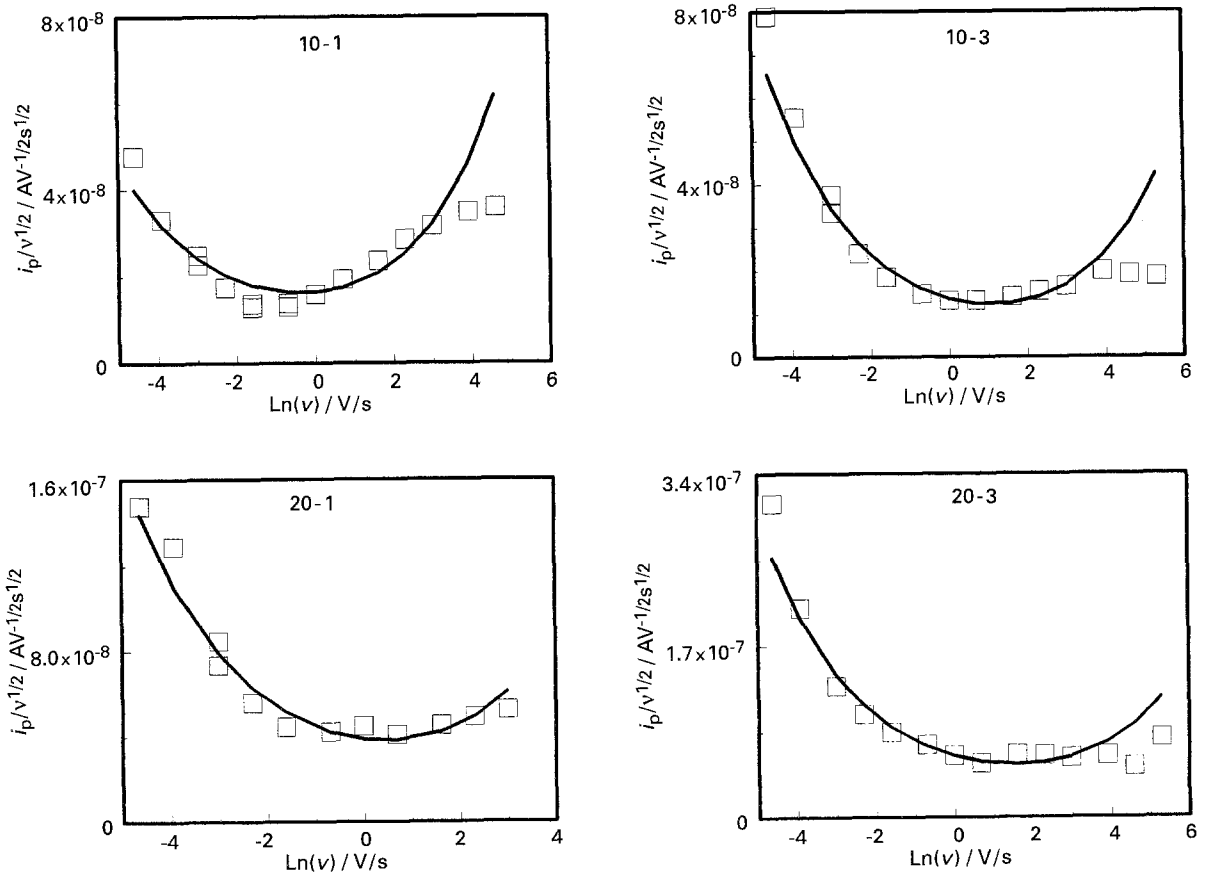

Fig. 11. The dependence of the maximum current function, $i_p/\nu^{1/2}$, on the scan rate, ν, for the iridium Microprobe electrodes. The squares represent the experimental data points and the solid lines correspond to Equation 12 derived from the regression analysis.

Table 10. Electrochemical characteristic dimensions of microprobe electrodes

Electrode ID	*Design electrode length, nl/μm*	*Electrochemically determined quantities based on diffusional mass transport*			*No mass transfer*
		Length, b/μm	*Radius, r/μm*	*Area, A/10⁶ cm²*	*Cavity volume, V/10⁹ cm³*
10–1	10	18 ± 8	4 ± 1	5 ± 2	3 ± 1
10–3	10	54 ± 1	0.4 ± 0.2	1.5 ± 0.7	1.6 ± 0.5
20–1	20	82 ± 18	1.5 ± 0.4	8 ± 1	5.1 ± 0.3
20–3	20	134 ± 36	1.9 ± 0.5	16 ± 2	4 ± 1

geometric areas. Altitude measurements determined from the voltammetric data at the lowest scan rates for these same electrodes suggest that the Parylene-C had peeled back from the iridium wire. The much larger exposed areas indicate that near the tip the degree of peeling is such that the cavity width is much greater than the diffusion layer thickness, δ, which is typically between 2 and 5 μm for an electrode radius of 1 μm and the other electrochemical conditions used. The data for the width of the cavity show that further down the electrode shaft the separation is of the order of 1 to 3 μm. The penetration depth, y, for all electrodes under these conditions is 25 to 250 times the radius of the electrode. The lengths of the cylinder from which the additional exposed area contributions arose suggest that the most extensive peeling was over a region between 20 and 130 μm. Consideration of all these dimensions suggest the petal like model for the electrode shown in Fig. 12.

From these results for this particular set of electrodes, the design and fabrication procedures of the stimulation electrodes do not provide the safe stimulation conditions previously thought to be achieved. It must be emphasized that the electrode dimensions determined for the Microprobe electrodes are approximate, bearing in mind the simplification made in the mathematical modelling. However, the purpose of the work is to develop evaluation protocols for the suitability of electrodes for neural stimulation and the results must be viewed in this context.

4. Conclusions

A procedure has been developed to evaluate the integrity of ultramicroelectrodes prior to their use in neural stimulation. The procedure is based upon the acquisition and interpretation of single cycle voltammetric curves obtained with and without depolarizer. On this basis it is shown that, for the small sample set of electrodes examined, imperfect seals between the conductor and the insulator, represent a major defect in the design and functionality of the electrode. Gross failures are readily detected by the asymmetry of the voltammetric curves obtained. Further, it is demonstrated that the presence of a minimum in the $i_p/\nu^{1/2}$ against ν plot, provides a diagnostic criterion to identify imperfect electrodes. For iridium ultramicroelectrodes produced by thin film technology, control of the morphology of the deposited metal is important to produce metal surfaces that can be converted uniformly into hydrated iridium oxide.

Consequently, two challenging problems must be resolved to achieve quality stimulation electrodes, and indeed any ultramicroelectrode, free from such defects.

(a) The bonding of the insulator to the conductor must be addressed in a systematic manner. Parylene-C is conveniently deposited by a vapour phase reaction on an ultramicroscale and can subsequently be removed incrementally to expose the working electrode. This work shows however that the Microprobe iridium electrodes are subject to serious failures due to the weak adhesion of this material to the iridium. In the case of resin formulations, thermal coatings of glasses and polymers and the application of thin films to produce metal oxide binding and insulation layers generally, the quality of the seal between conductor and insulator varies in different ways dependent on the procedure and is often determined by the skill of the fabricator, particularly as the perimeter to area ratio of the electrode increases.

(b) Although thin film technology produces well defined working surfaces attention to the homogeneity of the metal electrode surfaces as well as their crystallinity must be addressed. The present work shows that the surfaces on the UM electrode sites are porous and SEM measurement show that the

Table 11. The geometric surface area, GSA and the electrochemical dimensions of Microprobe and HMRI electrodes

Electrode	*10^6 GSA/cm²*	*10^6 A_{exp}/cm²*	*10^6 A_{cav}/cm²*	*λ/μm*	*y/μm*
IR300310A 10–1	0.54	4.7	10	3	40
IR300310A 10–3	0.35	1.5	6.5	2	200
IR300320A 20–1	2.5	7.5	39	1	400
IR300320A 20–3	1.9	16	59	1	500
HMRI-IC-06-02	4.77	4.8	7	0.3	10

A_{exp} freely accessible surface area of the electrode; A_{cav}, the electrode area within the cavity; λ, width of the cavity; y, the depth of the cavity.

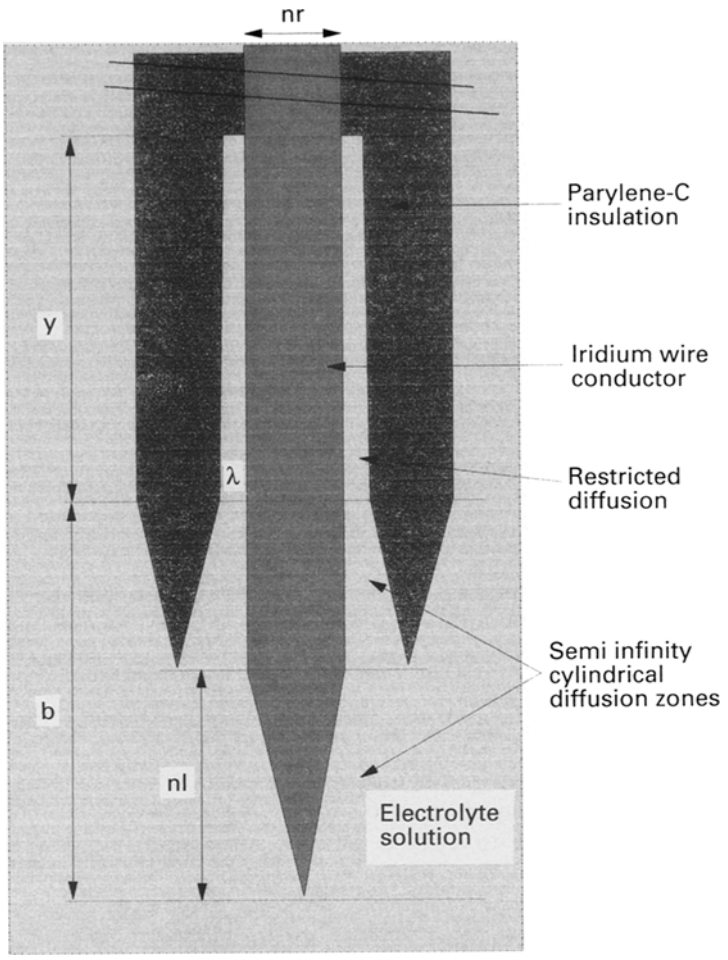

Fig. 12. A schematic representation of the Microprobe electrodes based upon their derived characteristic dimensions.

surface is heterogeneous since "the hillocks ... are from the underlying polysilicon conductor and not from the iridium" [17].

The presence of an imperfect seal or porous surface on a neural simulation electrode has serious consequences. The nonuniform current distributions that can arise in the presence of such defective structures (cracks, pores, or massive insulator detachment), alters the potentials at the metal–electrolyte interfaces in these defective regions in comparison to those expressed at the unconfined electrode interface. Electrochemical activation to form the hydrous iridium oxide can result in nonuniform coverage of the electrode with the oxide. The effective electrode area covered will depend on the method of activation and the frequency of the electrochemical modulation. Consequently, nonuniform current distribution will be present during stimulation pulsation. The charge injection capacities [20, 44, 45], measured conventionally, will not be meaningful for electrodes prepared under these conditions and severe tissue damage may result.

Acknowledgement

The author thanks S. H. White for the stimulating discussions during the development and preparation of this paper. The experiments were performed at EIC laboratories, under National Institute of Health, National Institute of Neurological Disorders and Stroke contracts NO1-NS-1-2300 and NO1-NS-8-2313 and grant 2 R44 NS26976-02.

References

[1] D. B. Cater and I. A. Silver, *in* 'Reference Electrode, Theory and Practice', (edited by D. J. G. Ives and G. J. Janz), Academic Press, New York (1961) p. 464.
[2] M. Fleischmann, S. Pons, D. R. Rolison and P. P. Schmidt, 'Ultramicroelectrodes', Datatech Systems, Science Publishers, Morganton, NC (1987).
[3] J. Heinze, *Ber. Bunsenges. Phys. Chem.* **85** (1981) 1096.
[4] K. B. Oldham, *J. Electroanal. Chem.* **122** (1981) 1.
[5] A. M. Bond and K. B. Oldham, *J. Electroanal. Chem.* **158** (1983) 193.
[6] R. M. Wightman, *Anal. Chem.* **53** (1981) 1125A.
[7] K. Aoki, K. Akimoto, K. Tokuda, H. Matsuda and J. Osteryoung, *J. Electroanal. Chem.* **171** (1984) 219.
[8] S. B. Brummer and M. J. Turner, *IEEE Trans. Biomed. Eng.* **24** (1977) 436.
[9] M. Bak, J. P. Girvin, F. T. Hambrecht, C. V. Kufta, G. E. Loeb and E. M. Schmidt, *Med. and Biol. Eng. and Comput.* **28** (1990) 257.
[10] B. E. Conway and E. Gileadi, *Trans. Faraday Soc.* **58** (1962) 2493.
[11] B. E. Conway, *Prog. Surf. Sci.* **16** (1984) 1.
[12] *Idem, J. Electrochem. Soc.* **138** (1991) 1539.
[13] B. E. Conway and J. Mazota, *Electrochim Acta* **28** (1983) 1.
[14] V. I. Birss, H. Elzanowska and S. Gottesfeld, *J. Electroanal. Chem.* **318** (1991) 327.
[15] M. Josowicz, J. Janata and M. Levy, *Proc. ECS PV* **87–89** (1987) 352.
[16] J. L. Anderson, *in* reference [2], p. 184.
[17] D. J. Anderson, K. Najafi, S. J. Tanghe, D. A. Evans, K. L. Levy, J. F. Hetke, X. Xue, J. J. Zappia and K. D. Wise, *IEEE Trans. Biomed. Eng. BME* **36** (1989) 693.

[18] D. R. Rolison, *in* reference [2], p. 65.
[19] A. J. Ribes and J. Osteryoung, *in* 'Microelectrodes: Theory and Applications' (edited by M. I. Montenegro, M. A. Queiros and J. L. Daschbach), Kluwer Academic Publishers, Boston (1991) p. 259.
[20] D. B. McCreery, W. F. Agnew, T. G. H. Yuen and L. Bullara, *IEEE Trans. Biomed. Eng.* **37** (1990) 996.
[21] *Idem*, HMRI Quarterly Progress Report Q1 (1983), Contract NO1-NS-0-2317.
[22] M. Salcman and M. J. Bak, *Med. Biol. Eng.* **14** (1976) 42.
[23] G. E. Loeb, M. J. Bak, M. Salcman and E. M. Schmidt, *IEEE Trans. Biomed. Eng.* **24** (1977) 121.
[24] D. T. Sawyer and J. R. Roberts, 'Experimental Electrochemistry For Chemists', Wiley, New York (1974) pp. 74–78.
[25] K. B. Oldham, *J. Electroanal. Chem.* **323** (1992) 53.
[26] *Idem, ibid.* **237** (1987) 303.
[27] K. B. Oldham and C. G. Zoski, *ibid.* **256** (1988) 11.
[28] Y. Saito, *Rev. Polarogr. (Jpn.)* **15** (1968) 177.
[29] A. M. Bond, K. B. Oldham and C. G. Zoski, *J. Electroanal. Chem.* **245** (1988) 71.
[30] R. M. Penner, M. J. Heben, T. L. Longin and N. S. Lewis, *Science* **250** (1990) 118.
[31] C. G. Zoski, A. M. Bond, C. L. Colyer, J. C. Myland and K. B. Oldham, *J. Electroanal. Chem.* **263** (1989) 1.
[32] C. G. Zoski, A. M. Bond, C. L. Colyer, J. C. Myland and K. B. Oldham, *J. Electroanal. Chem.* **263** (1989) 1 (see reference 24 therein).
[33] U. M. Twardoch, unpublished work (1993).
[34] K. R. Wehmeyer and R. M. Wightman, *J. Electroanal. Chem.* **196** (1985) 417.
[35] A. J. Bard and L. R. Faulkner, 'Electrochemical Methods', Wiley, New York (1980).
[36] K. Fox, M. Armstrong-James and J. Millar, *J. Neurosci. Methods* **3** (1980) 37.
[37] F. A. Posey and T. Morozumi, *J. Electrochem. Soc.* **113** (1966) 176.
[38] A. M. Johnson and J. Newman, *ibid.* **118** (1971) 510.
[39] W. Tiedemann and J. Newman, *ibid.* **122** (1975) 70.
[40] I. G. Goldberg, A. J. Bard and S. F. Feldberg, *J. Phys. Chem.* **76** (1972) 2550.
[41] I. G. Goldberg and A. J. Bard, *J. Electroanal. Chem.* **38** (1972) 313.
[42] R. S. Nicholson and I. Shain, *Anal. Chem.* **36** (1964) 706.
[43] K. Aoki, K. Honda, K. Tokuda and H. Matsuda, *J. Electroanal. Chem.* **182** (1985) 267.
[44] L. S. Robblee, J. L. Lefko and S. B. Brummer, *J. Electrochem. Soc.* **130** (1983) 731.
[45] L. S. Robblee and T. R. Rose, *IEEE Trans. Biomed. Eng.* **37** (1990) 1470.